Failure mode change and material damage with varied machining speeds: a review

OPEN ACCESS
IOP Publishing | IMMT
International Journal of Extreme Manufacturing
Int. J. Extrem. Manuf. **5** (2023) 022003 (25pp)
https://doi.org/10.1088/2631-7990/acbd6f

Topical Review

Failure mode change and material damage with varied machining speeds: a review

Jianqiu Zhang, Binbin He and Bi Zhang*

Department of Mechanical and Energy Engineering, Southern University of Science and Technology, Shenzhen 518055, People's Republic of China

E-mail: zhangb@sustech.edu.cn

Received 10 October 2022, revised 20 December 2022
Accepted for publication 19 February 2023
Published 17 March 2023

Abstract

High-speed machining (HSM) has been studied for several decades and has potential application in various industries, including the automobile and aerospace industries. However, the underlying mechanisms of HSM have not been formally reviewed thus far. This article focuses on the solid mechanics framework of adiabatic shear band (ASB) onset and material metallurgical microstructural evolutions in HSM. The ASB onset is described using partial differential systems. Several factors in HSM were considered in the systems, and the ASB onset conditions were obtained by solving these systems or applying the perturbation method to the systems. With increasing machining speed, an ASB can be depressed and further eliminated by shock pressure. The damage observed in HSM exhibits common features. Equiaxed fine grains produced by dynamic recrystallization widely cause damage to ductile materials, and amorphization is the common microstructural evolution in brittle materials. Based on previous studies, potential mechanisms for the phenomena in HSM are proposed. These include the thickness variation of the white layer of ductile materials. These proposed mechanisms would be beneficial to deeply understanding the various phenomena in HSM.

Keywords: high-speed machining, adiabatic shear band, subsurface damage, dynamic recrystallization

1. Introduction

High-speed machining (HSM) has considerable potential in various industries because it is highly efficient and saves energy [1]. The concept of HSM was proposed by Salomon who stated that the machining temperature initially increased and then decreased with increasing machining speed [2]. However, over the last several decades, many debates over Salomon's assumption have ensued [3]. This article sets aside these arguments and focuses on the underlying mechanisms of various phenomena in both HSM and ultrahigh-speed machining (UHSM) in terms of solid mechanics and material science. In HSM, the occurrence of adiabatic shear band (ASB) is an important phenomenon that intrinsically results from material instabilities. Another vital phenomenon is shock. Although generally ignored by researchers, shock occurs at a machining speed of approximately 1000 m s^{-1} based on the

* Author to whom any correspondence should be addressed.

molecular dynamics (MD) simulation conducted. Because the machining speed that causes shock usually reaches the order of 1000 m s^{-1}, in this study, the speed range of HSM is set to less than 1000 m s^{-1}, and that of UHSM exceeds 1000 m s^{-1} for simplicity.

Zener and Hollomon discovered the ASB in the 1940s [4]. Its mechanical framework, named as ASB onset system, was established by Wright and Batra in the 1980s [5]. The mechanical framework was subsequently modified by many researchers to define more applicable systems [6–13] for HSM. By applying appropriate boundary and initial conditions, these systems can be solved using numerical methods, such as the finite difference method. Additionally, these systems can be handled by the perturbation method to establish ASB onset criteria [8, 11, 13–16]. These criteria are convenient to assess if the ASB occurs under specific conditions. This topic is discussed in detail in section 2.1.4.

In these ASB onset systems, constitutive models are vital and responsible for describing the material deformation behavior. In HSM, material deformation behavior is depicted by thermo-visco-plastic constitutive models that typically consider the strain, strain rate, and temperature to predict stress. Constitutive models can be divided into two categories: empirical and physical. The former exhibits a coupling pattern between the strain, strain rate, and temperature. The latter is built from bottom to top, involving material activities at the atomistic scale (e.g. dislocation dynamic behavior) [17]. Specifically, when the strain rate is lower than 10^4 1 s^{-1}, the constitutive models are dominated by dislocation thermal activation [18]. When the strain rate is in the range 10^4–10^7 1 s^{-1}, the constitutive models are mainly influenced by phonon drag [19–22]. Nevertheless, in this strain rate range, some researchers suppose that the multiplication of the geometric dislocation density must be the governing factor in the constitutive models [23]. Further, when the strain rate exceeds 10^7 1 s^{-1}, the relativistic effect plays the most vital role in the constitutive models.

A typical ASB failure in ductile materials results from void evolution. Researchers have investigated the contribution of void evolution to material failure. Among the well-known articles is Gurson's work [24], which was the first to introduce micro-void fraction in material behavior. Subsequently, because void fraction was attributed to void nucleation and growth, some researchers started to focus on the law for void nucleation and growth. In 1976, Seaman *et al* [25] described void nucleation and growth. In 1984, Gurson's model was improved by Tvergaard and Needleman through a finer characterization of void nucleation and growth [26]. With advancements in numerical computational power, many researchers performed finer studies [27–31] using MD to reveal the underlying mechanism triggering void evolution. The MD results showed that complex dislocation activities caused void evolution. However, these results were challenged by Nguyen and Warner [32]. They contradicted the conventional viewpoint that stress triaxiality causes void growth [33, 34].

Various types of damage are caused by thermomechanical coupling in HSM. For ductile crystalline equiaxed fine grains (EFGs) [35], plastic deformation and micro-voids are the major types of damage occurring at the mesoscale in HSM. The evolution of these types of damage is related to dislocations, twinning, and phase transformation [36–38] at the atomistic scale. These types of damage at the mesoscale frequently occur within the ASBs of chips or in the subsurface [39–41]. For brittle materials, cracks, stacking faults and amorphization are the major damage types in the subsurface [42–44]. In HSM, cracks initialize in the high-pressure zone, and propagate to deeper and lateral locations. In HSM, except for the cracks in brittle materials, the damage to both ductile and brittle materials is the result of thermomechanical coupling [35, 45, 46]. These types of damage are introduced in section 3.

We acknowledge the efforts of the researchers who published reviews over the past several decades. These reviews focused on many aspects of HSM, including manufacturing equipment and processes [47, 48], manufacturing processes on specific materials [49, 50], material property changes [51, 52], subsurface damage [53], and HSM advancement [54]. To the best knowledge of the authors, a comprehensive review of HSM and UHSM in solid mechanics and material science is lacking. The first part of this paper reviews the solid mechanics of ASB onset and failure in HSM. Specifically, physical constitutive equations and dynamic dislocation gliding are highlighted. Then, a novel finding, the transition from ASB to shock, is discussed based on the MD simulation conducted by the authors. In the second part, various types of damage to both ductile and brittle materials in HSM were analyzed. In addition, because the current machining speed cannot reach the critical speed resulting in shock, the damage caused by one-dimensional (1D) shock is instead reviewed to compensate for the foregoing deficiency. Owing to a limited space, a few topics regarding solid mechanics and material damage in HSM, including ASB spacing [55], residual stress in the subsurface, surface hardness, and roughness, were not discussed. Besides, nanoscale effects were not included either [56, 57].

2. Solid mechanics description of ASB and shock

2.1. Mechanics of dynamic shear

2.1.1. Dynamic dislocation gliding. The underlying metallurgical activities of plastic strain at the mesoscale are mainly those of dislocation evolution. Among the various dislocation evolutions, dislocation gliding is the major activity at a relatively low strain rate. Compared with other activities, such as dislocation climbing and dislocation nucleation, dislocation gliding requires lower stress. When the dislocation velocity is relatively low, thermal activation is the core mechanism for dislocation gliding. In this section, the core mechanisms are introduced as they have been widely utilized by physics-based constitutive models.

The stress that resists dislocation gliding can be classified into two parts: athermal and thermal. The total resistant stress can be given by stress superposition, as follows:

$$\tau = \tau_{\mathrm{ath}} + \tau_{\mathrm{th}}, \tag{1}$$

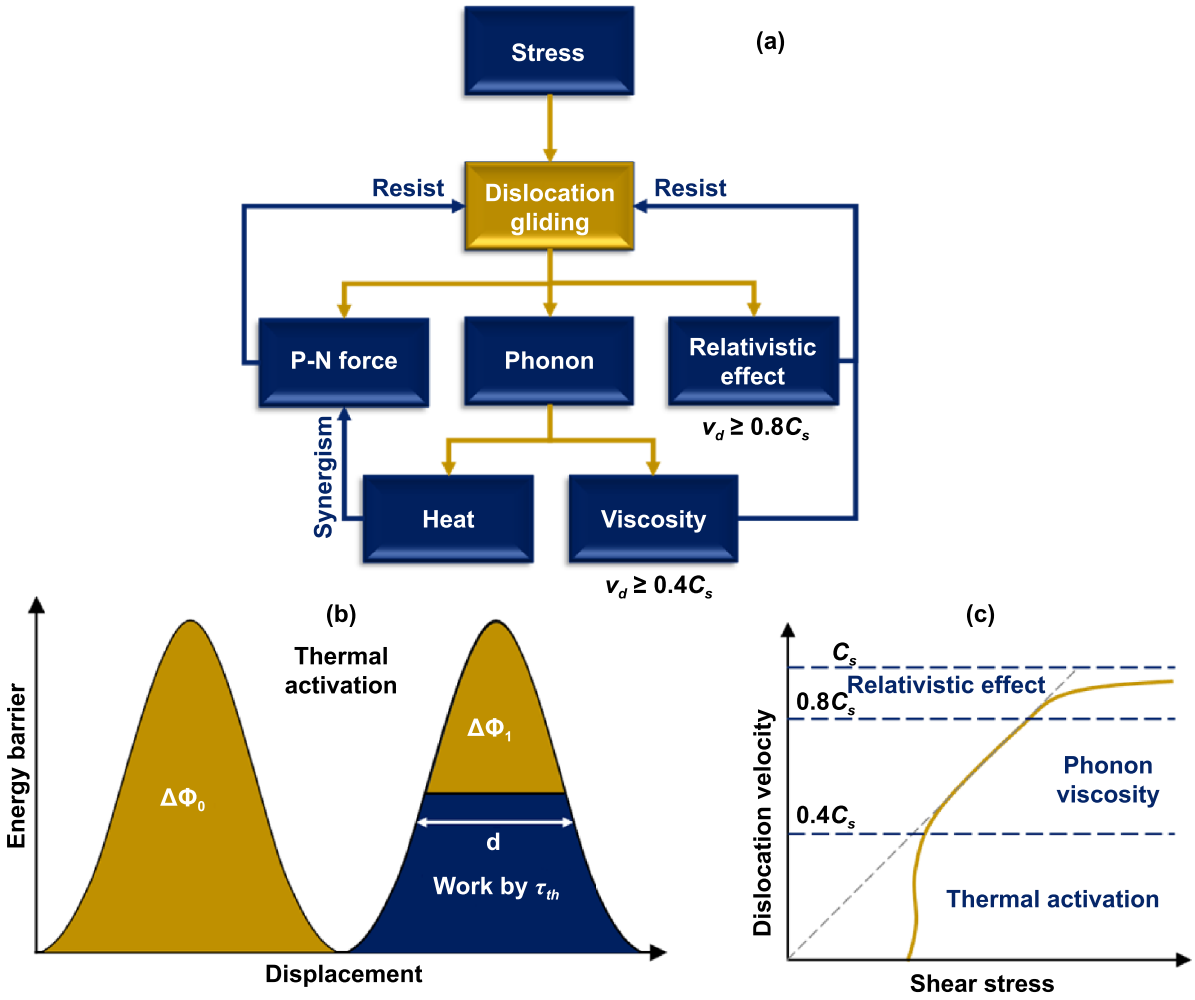

Figure 1. Various mechanisms in dislocation gliding: (a) three factors reversely affecting dislocation gliding; (b) energy barrier overcome by thermal activation mechanism; (c) three factors influencing shear stress at distinct strain rate ranges (Reprinted from [17], Copyright (1987), with permission from Elsevier).

where τ is the shear stress; τ_{ath} is the athermal stress caused by the long-range interactions among atoms; and τ_{th} is the short-range stress relative to the thermal effect. Specifically, τ_{th} can be further classified into three types of interactions, as shown in figure 1(a): Peierls–Nabarro force [58, 59] influenced by thermal activation, viscous force induced by the phonon drag mechanism, and relativistic force interpreted by relativistic inertia. These resistant forces play important roles at distinct strain rate ranges. When the dislocation velocity is lower than 40% of the elastic shear wave speed, C_S, the thermal activation mechanism is the main contributor to resistance [17]. The viscous force must be considered, and the thermal activation mechanism can be neglected when the dislocation velocity exceeds $0.4C_S$. The relativistic force must be considered when the dislocation velocity exceeds $0.8C_S$. The contributions of the three factors to stress are shown in figure 1(c). The dislocation velocities of $0.4C_S$ and $0.8C_S$ approximately correspond to strain rates of 10^4 and 10^8 1 s^{-1}, respectively.

Dislocation gliding requires atoms to construct dislocations for overcoming energy barriers along the gliding path. These energy barriers originate from atom interactions and can be overcome by the synergism between stress work and thermal fluctuation. As shown in figure 1(b), the total energy barrier is $\Delta\Phi_0$. If shear stress is absent, the energy barrier to be overcome is the total energy. Once shear stress is applied, $\Delta\Phi_1$ remains as the residual energy barrier overcome by thermal fluctuations. Therefore, the energy barrier can be divided into two parts:

$$\Delta\Phi_0 = \Delta\Phi_1 + W_{\mathrm{shear}}, \tag{2}$$

where W_{shear} is the work done by shear stress. Theoretically, the thermal fluctuation energy depends on the vibration frequency of the atoms causing the dislocations. This relationship can be described by an equation in Arrhenius form, as follows [60]

$$\nu_1 = \nu_0 \exp\left(-\frac{\Delta\Phi_1}{k\theta}\right), \tag{3}$$

where ν_0 is the atom vibration frequency at 0 K; ν_1 is the atom vibration frequency successfully overcoming an energy barrier at temperature θ; and k is the Boltzmann constant.

Because ν_1 is the frequency at which an energy barrier is successfully overcome, $1/\nu_1$ is the time consumed for successfully overcoming a barrier. As shown in figure 1(b), the average barrier width, d, can be expressed as $d = v_1/\nu_1 = v_0/\nu_0$, where v_1 and v_0 are the average velocities of dislocations at θ and 0 K, respectively. Subsequently, the two frequencies in equation (3) can be replaced by velocity (i.e. $v_1 = v_0 \exp(-\Delta\Phi_1/k\theta)$). Recall that the Orowan equation is a power tool that can bridge the strain rate at the macroscale and dislocation velocity through the form

$$\dot{\gamma} = \frac{1}{M}\rho_d b v_d, \tag{4}$$

where $\dot{\gamma}$ is the shear strain rate; ρ_d is the dislocation density; b is Burgers vector; v_d is the dislocation velocity; and M is a constant relative to the angle between the direction of the shear strain and dislocation velocity. Furthermore, the velocity in the Arrhenius equation, $v_1 = v_0 \exp(-\Delta\Phi_1/k\theta)$, can be replaced by the strain rate expressed in equation (4). Then, the Arrhenius equation becomes

$$\dot{\gamma}_1 = \dot{\gamma}_0 \exp\left(-\frac{\Delta\Phi_1}{k\theta}\right), \tag{5}$$

where $\dot{\gamma}_0$ is the reference strain rate at 0 K. The relationship between strain rate $\dot{\gamma}$ and temperature θ is clarified by equation (5). By inserting equations (5) into equation (2) and rewriting the shear stress work in terms of shear stress, the total energy barrier can be given by [61]

$$\Delta\Phi_0 = k\theta \ln\left(\frac{\dot{\gamma}_0}{\dot{\gamma}}\right) + bld\tau_{\text{th}}, \tag{6}$$

where b is Burgers vector, and l is the length of the dislocation line. Conventionally, the variables in front of τ_{th} in the last term, bld, is the thermal activation volume; however, the activation volume is not a real volume in the three-dimensional space.

Equations (3), (5), and (6) in Arrhenius form are the core concepts for constructing various physics-based constitutive equations, including the mechanical threshold stress model [20] and the Wedberg–Lindgren model [62]. Thermal activation volume is another widely used concept. It is adopted by another set of physics-based constitutive equations, such as the Zerilli–Armstrong [63] and Gao–Zhang models [23].

The thermal activation model is associated with the relationship between heat and stress. The essence of heat is the stochastic vibration of atoms. After one dislocation structure gliding by the atoms that construct itself, the atoms are stimulated to vibrate intensely, generating local heat. When the dislocation glide speed increases, the adiabatic effect gradually plays a significant role because the vibrations of the atoms constructing dislocations cannot be transferred to a more distant field over a short time.

For the cases where the dislocation velocity exceeds $0.4C_S$, the viscous force and relativistic effect play vital roles that dominate dislocation gliding. The influence of the two factors can be summarized into one equation in general form:

$$ma + Bv_d + F_r = F_{\text{ap}}, \tag{7}$$

where $m = m_0/\sqrt{1 - v_d^2/C_S^2}$ (m_0 is the equivalent mass, and C_S is the elastic shear wave speed); B is the viscous damping coefficient; F_r is the force resolved by the tension in the dislocation opposite to the direction of F_{ap}; and F_{ap} is the applied stress. The first term on the left side of equation (7) is inertia, which is only effective when the strain rate exceeds $0.8C_S$. Because dislocation is a structure and not a mass, the effective mass is not a property of dislocation. One possible explanation is that the relativistic effect originates from the inertia of atoms that construct dislocations. When a dislocation accelerates to an extremely high speed to overcome one barrier, atom inertia resists the accelerating activities. Consequently, resistance is considered as a relativistic effect. The second term on the left-hand side of equation (7) can be derived from the viscous effect: the process of overcoming one barrier provides kinetic energy to the atoms involved. The kinetic energy dissipates in the form of crystalline vibration (also called phonons in quantum mechanics). As shown in figure 1(a), the phonons have two main effects. One is the heat that assists the dislocation in overcoming the barrier results in a faster dislocation motion. The other is viscous damping drags the dislocation motion when the velocity exceeds $0.4C_S$. The third term on the left-hand side of equation (7) is caused by the tension in the dislocation line. In typical dislocation motions, the dislocation is driven by shear stress and exhibits a bow shape owing to the pinning on two sides. The tension in the bow-shaped dislocation line can be resolved in a direction opposite to that of the applied stress.

2.1.2. Constitutive equations. When the strain rate is lower than 10^4 1 s^{-1}, thermal activation is the core mechanism on which physics-based constitutive equations are established. One relationship obtained from the experiments is typically used to express the remaining energy barrier:

$$\Delta\Phi_1 = \mu b^3 g_0 \left[1 - \left(\frac{\tau}{\tau_0}\right)^p\right]^q, \tag{8}$$

where p and q are factors that describe the shape of the energy barrier; μ is the shear modulus depending on the temperature; and g_0 is the normalized total activation energy. By inserting equation (5), which describes the thermal activation in equation (8), the mechanical threshold stress model [20] is given by

$$\tau_{\text{th}} = \tau_{\text{th0}}\left[1 - \left(\frac{k\theta}{\mu b^3 g_0}\ln\frac{\dot{\gamma}_0}{\dot{\gamma}}\right)^{1/q}\right]^{1/p}. \tag{9}$$

Several other physics-based constitutive equations were built in a similar manner, combining some other empirical or physical equations with equation (5). For instance, Hoge and Mukherjee [64] suggested that dislocations glide on a slip plane by forming kink pairs. The activation energy equation of the kink pair is in the form of equation (5). The Hoge–Mukherjee model is built based on the activation-energy equation of the kink pair by including another relationship between thermal activation and flow stress.

Table 1. Mechanisms and strain rate ranges of physics-based constitutive equations.

Constitutive equations	Major mechanisms	Strain rate ranges (1 s^{-1})
Mechanical threshold stress [20]	Thermal activation	$\dot{\varepsilon} < 10^4$
Hoge–Mukherjee [64]	Thermal activation Viscous dragging	Not explicitly confirmed
Gao–Zhang [23]	Thermal activation for $\dot{\varepsilon} < 10^4$ Dislocation multiplication for $\dot{\varepsilon} > 10^4$	$\dot{\varepsilon} < 10^5$
Steinberg–Lund [65]	Thermal activation	$\dot{\varepsilon} < 10^6$
Wedberg–Lindgren [62]	Thermal activation Viscous dragging	Not explicitly confirmed
Zerilli–Armstrong (1992) [19]	Thermal activation Viscous dragging	$\dot{\varepsilon} < 10^4$
Zerilli–Armstrong [63]	Arrhenius form	$\dot{\varepsilon} < 10^4$

Among a few physics-based constitutive equations, the Gao–Zhang model [23] is special because it may be the only model that adopts the dislocation density increase as the mechanism for interpreting the sharp stress increase when the strain rate exceeds 10^4 1 s^{-1}. As mentioned, phonon drag is the main contributor to stress when the strain rate exceeds 10^4 1 s^{-1}. However, the experiments conducted by Follansbee and Kocks [20] offered another possible mechanism for the stress increase at a strain rate of 10^4 1 s^{-1}. In the tensile experiments, the copper specimen exhibited a sharp strain increase when the strain rate was 10^4 1 s^{-1}. The sharp strain increase implies a sharp increase in the dislocation density at the microscale. This result was confirmed by Zerilli and Armstrong [19]. Thus far, the mechanism of the stress increase at a strain rate of 10^4 1 s^{-1} is vague. Another possible reason is that both dislocation multiplication and phonon drag contribute to the sharp increase in stress. The phonon drag mechanism is corroborated by the results of theoretical dislocation dynamics [13]. For quick reference, a few physics-based constitutive equations are listed in table 1.

For the above equations, no solid evidence proving that one of them is better than the others. All these equations are based on the dislocation dynamics theory. Nevertheless, in the real world, microstructural evolution is considerably more complex than ideal assumptions in constitutive models. For instance, in the ASBs of steel, microstructural evolution includes phase transformation, dynamic recrystallization (DRX), and twinning. The dislocation density in EFGs caused DRX was extremely low. In the DRX process, the dislocations in the original large grains were released to the grain boundaries to form EFGs; such a DRX process is not included to any one of these physics-based models.

These microstructures reciprocally strengthen materials, including dislocation, twinning, and phase transformation. The intersections among massive dislocations form multijunctions that build dislocation nets, which cause glissile dislocations to settle, forming sessile dislocations. Consequently, the dislocation density increases to form a dislocation forest. High dislocation densities cause strain hardening that strengthens materials. A famous material strengthening law is the Taylor hardening law, which presents that flow stress is proportional to the square root of dislocation density [66]. The strengthening mechanism of twinning and phase transformation can be introduced by two classical effects, twinning-induced plasticity (TWIP) and phase-transformation-induced plasticity (TRIP). The two effects are often seen in steel. TWIP steel has low stacking fault energy resulting in isolated stacking faults and twinning [67]. Dislocation evolution is still the major mechanism in the plastic deformation of TWIP. Massive twinning planes are the energy barriers resisting dislocation gliding. Therefore, the similarity of TWIP and dislocation forests is that material strengthening is obtained by increasing the number of energy barriers for dislocation gliding. More energy barriers shorten the free-moving path of the gliding of glissile dislocations. In consequence, the plastic flow is confined, and flow stress is elevated. The strengthening mechanism of TRIP is different from the previous two. The phase transformation from soft to hard phase in loading is the strengthening mechanism of TRIP [68]. The phase transformation from Ferrite to martensite is frequently seen in TRIP steel.

The other category includes empirical constitutive models. The most famous among them is the Johnson–Cook (J–C) model [69] because of its simple form and frequent use in engineering. Notably, the logarithmic form of the strain rate term in the J–C model is similar to the form of the strain rate in equation (6). Such a pattern balances its simplicity and effectiveness. This is possibly the reason for the wide application of the J–C model. Another empirical model, the Klopp–Clifton–Shawki model, must be mentioned because it has the simplest form among all the models [70]. This model is constructed by the simple coupling of a set of exponential functions in terms of strain, strain rate, and temperature, rendering it extremely convenient for mathematical operations. This model was adopted by several researchers in the stability analysis of ASB [13, 71, 72]. For convenience, other empirical constitutive equations can be found in the article of Yang and Zhang [51].

2.1.3. Governing systems of ASB onset. Shear failure is a widely considered failure mechanism of ductile materials. In HSM, this mechanism still holds. Specifically, in the HSM, shear damage is concentrated on a narrow band to form an ASB, which is caused by the intrinsic instability of the material. In terms of solid mechanics, the ASB can be

simplified into a 1D model that allows field variables (including temperature, strain, strain rate, and stress) to vary along the width direction of the ASB. This simplification is reasonable because the field variables considerably change in the width direction but remain steady in the slipping direction. Based on Wright's theoretical framework [73], a general form of the description can be given by an ASB onset system consisting of partial differential equations:

$$\begin{cases} \frac{\partial \tau}{\partial y} = \rho \frac{\partial v_x}{\partial t} & \text{momentum} \\ \rho C_{\mathrm{V}} \frac{\partial \theta}{\partial t} = \kappa \frac{\partial^2 \theta}{\partial y^2} + \beta \tau \frac{\partial \gamma_{\mathrm{p}}}{\partial t} & \text{energy} \\ \frac{\partial \gamma}{\partial t} = \frac{\partial}{\partial t}\left(\frac{\partial u_x}{\partial y}\right) = \frac{\partial v_x}{\partial y} & \text{geometry} \\ \frac{\partial \tau}{\partial t} = \mu\left(\frac{\partial v_x}{\partial y} - \frac{\partial \gamma_{\mathrm{p}}}{\partial t}\right) & \text{elasticity} \\ \frac{\partial \gamma_{\mathrm{p}}}{\partial t} = f(\tau, \kappa, \theta) & \text{plastic flow} \\ \frac{\partial \psi}{\partial t} = \xi(\tau, \kappa, \theta) & \text{material hardening} \end{cases}, \quad (10)$$

where v_x is the material velocity along the x direction; u_x is the displacement along the x direction; y is a coordinate; γ_{p} is the plastic shear strain; γ is the shear strain; ρ is the material density; t is time; κ is the thermal conductivity; C_{V} is the volumetric heat capacity; ψ is material hardening; and β is the Taylor–Quinney coefficient. The ASB onset system (i.e. equation (10)) is a general form that can be concretized into distinct applications. Over the past two decades, a few specific systems describing the ASB in HSM have evolved from system (10).

In 1997, the ASB onset system for serrated chips was built by Davies *et al* [6]. It is given by

$$\begin{cases} \frac{\partial \tau}{\partial y} = \frac{\sigma}{h} & \text{momentum} \\ \rho C_{\mathrm{V}} \frac{\partial \theta}{\partial t} = \kappa \frac{\partial^2 \theta}{\partial y^2} + \tau \frac{\partial v_x}{\partial y} & \text{energy} \\ \frac{\partial \gamma}{\partial t} = \frac{\partial}{\partial t}\left(\frac{\partial u_x}{\partial y}\right) = \frac{\partial v_x}{\partial y} & \text{geometry} \\ \tau = f(\gamma, \dot{\gamma}, \theta) & \text{constitutive} \end{cases}, \quad (11)$$

where h is the uncut depth, and σ is the normal stress in the ASB induced by cutter loading. The comparison of systems (11) and (10) indicates that the equation describing the elasticity in system (10) is omitted. This is because elastic behavior typically occurs within a small strain range compared with that of plastic strain. In HSM, such a small strain range can be neglected. Additionally, the plastic flow and material hardening in system (10) are replaced by the constitutive equation in system (11). This is because thermo-visco-plastic constitutive models are capable of describing the material behavior (including plastic flow and material hardening). Notably, the normal stress from the cutter tip was considered in the momentum equation, which implies that a complex stress state causes the ASB onset in HSM. Nevertheless, the inertial term was omitted in the momentum equation of system (11). Consequently, system (11) is only applied to cases with a relatively low machining speed. The improvement of system (11) is that the normal stress in HSM is considered.

More sophisticated systems have been proposed by Ma *et al* [9], Cai and Dai [10], and Ye *et al* [11, 16] in the recent decade. The research of Ma *et al* focused on the shear stresses at the junction of the primary shear zone (PSZ) and secondary shear zone (SSZ). Therefore, the 1D ASB onset system was expanded into a two-dimensional system based on the plane strain assumption. The system is given by

$$\begin{cases} \frac{\partial^2 \varepsilon_{xy}}{\partial t^2} = \frac{\partial^2 (\sigma_x + \sigma_y)}{\partial x \partial y} + \frac{\partial^2 \tau_{xy}}{\partial x^2} + \frac{\partial^2 \tau_{xy}}{\partial y^2} & \text{momentum} \\ \rho C_{\mathrm{V}} \frac{\partial \theta}{\partial t} = \kappa\left(\frac{\partial^2 \theta}{\partial x^2} + \frac{\partial^2 \theta}{\partial y^2}\right) + \beta\left(\tau_{xy}\dot{\varepsilon}_{xy} + \sigma_x \dot{\varepsilon}_x + \sigma_y \dot{\varepsilon}_y\right) & \text{energy} \\ \frac{\partial^2 \varepsilon_x}{\partial y^2} + \frac{\partial^2 \varepsilon_x}{\partial y^2} - \frac{\partial^2 \varepsilon_{xy}}{\partial x \partial y} = 0 & \text{geometry} \\ \tau = f(\gamma, \dot{\gamma}, \theta) & \text{constitutive} \end{cases}, \quad (12)$$

where σ_x, σ_y, τ_{xy}, ε_x, ε_y, and ε_{xy} denote the normal stress along the x direction, normal stress along the y direction, shear stress, normal strain along the x direction, normal strain along the y direction, and shear strain, respectively. Any quantity with the dot ('·') at the top denotes the time differential of the quantity. System (12) offers an approach to mimic the complex stress state in front of a cutter tip because of the overlap of PSZ and SSZ.

In 2014, Cai and Dai [10] developed an apparatus for depressing ASBs in machining by setting a constraint that renders the cutter resembling a wood planer. A constraint against the rake face compressed the ASB along the ASB slipping direction. Compression depresses ASB growth. In the system of solid mechanics, the compressive normal stresses exerted by the constraint and rake face are considered. Therefore, two compressive stress terms are involved in the momentum equation. Additionally, the influence of material convection within the ASB is involved in the energy equation of the system because material convection affects the heat transfer in the system.

In 2018, Ye *et al* [16] established a comprehensive system in which material convection contributed to strain and heat. The compressive stress induced by the cutter tip on the ASB was assumed to decrease linearly toward the free surface where the compressive stress became zero. The information on the ASB described by the system is illustrated in figures 2(a) and (b). As shown in figure 2(a), the ASB occurs at the PSZ when the cutter moves at a constant cutting speed, V_0. The normal stress induced by the cutter tip and the direction of material convection are shown in figure 2(b). The corresponding system is given by

$$\begin{cases} \frac{\partial^2 \tau}{\partial y^2} + \frac{\xi \sin\varphi}{b}\sigma = \rho \frac{\partial^2 \gamma}{\partial t^2} & \text{momentum} \\ \rho C_{\mathrm{V}} \frac{\partial \theta}{\partial t} = \beta \tau\left(\frac{\partial \gamma}{\partial t} + V_f \frac{\partial \gamma}{\partial y}\right) + \kappa \frac{\partial^2 \theta}{\partial y^2} - \rho C_{\mathrm{V}} V_f \frac{\partial \theta}{\partial y} & \text{energy} \\ \frac{\partial^2 \sigma}{\partial t \partial y} + V_f \frac{\partial^2 \sigma}{\partial y^2} = -\frac{E}{\delta}\left(\frac{\partial \gamma}{\partial t} + V_f \frac{\partial \gamma}{\partial y}\right) (\mathrm{un}) & \text{loading} \\ \frac{\partial \gamma}{\partial t} = \frac{\partial}{\partial t}\left(\frac{\partial u_x}{\partial y}\right) = \frac{\partial v_x}{\partial y} & \text{geometry} \\ \tau = f(\gamma, \dot{\gamma}, \theta) & \text{constitutive} \end{cases}, \quad (13)$$

where $\xi = 1 + \mu \tan(\alpha - \varphi)$ is a constant depending on the shear and rake angles, φ and α, respectively; σ is the normal stress caused by cutter compression; V_f is the convection velocity; E is Young's modulus; and δ is the ASB length. In system (13), the second term, $(\xi \sin\varphi / b)\sigma$, of the momentum equation is attributed to the compressions due to the cutter.

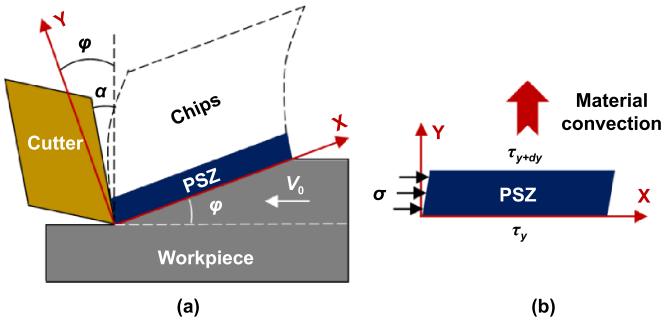

Figure 2. ASB occurrence at PSZ: (a) geometric information of ASB in PSZ and (b) normal stress induced by cutter tip and material convection direction.

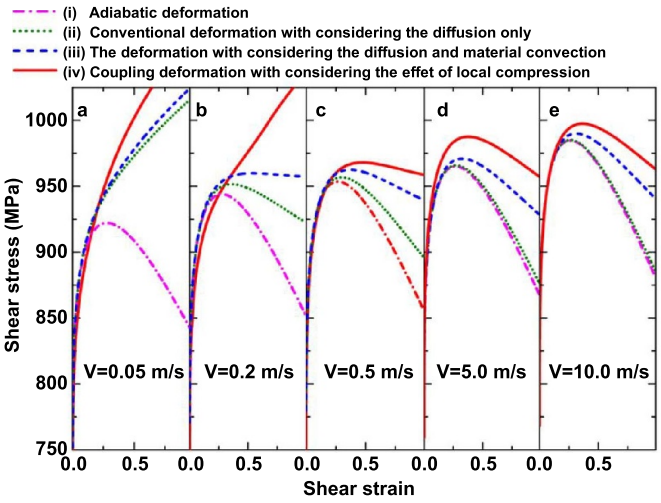

Figure 3. Stress–strain history in ASB at various machining speeds (Reprinted from [16], Copyright (2018), with permission from Elsevier).

The third term on the right side of the energy equation is the heat removed by material convection; the '(un)loading' equation is formulated based on the chip loading-unloading process. This equation is a compensative equation due to the extra introduced variable, σ.

In the systems discussed above, the constitutive equation is given in a general form. Ye *et al* [16] replaced the constitutive equation of system (13) with the 1D J–C model and provided the numerical solutions to Ti6Al4V through the finite difference method based on Euler's coordinates, as shown in figure 3. This figure presents the solutions of the four cases for comparison. Case (i) is an adiabatic case in which heat diffusion and material convection are prevented. Case (ii) involves heat diffusion, and case (iii) includes the effect of both heat diffusion and material convection, which can be formulated by leaving the corresponding terms in system (13). As shown in figure 3, an ASB onset can be determined by engineering criteria:

$$\text{Criterion 1}: \frac{\partial \tau}{\partial \gamma} \leqslant 0. \tag{14}$$

Criterion 1 demonstrates that the ASB onset starts at the location where the slope of the curve is zero. The ASB onset occurs in case (i) even at the lowest machining speed. Nevertheless, the ASB onset in case (iv) requires the highest machining speed than the other cases. This is because heat diffusion and material convection dissipate local heat. Hence, to provide higher transient local heat, the ASB onset requires a higher machining speed. In addition, compression causes high hydrostatic stress, which negatively affects the onset of ASB.

2.1.4. ASB instability. Section 2.1.3 demonstrates that the ASB onset can be determined by solving the system. This onset can be explicitly obtained by applying the perturbation method to the system. For example, the system of case (ii) in figure 3 is given by

$$\begin{cases} \frac{\partial \tau}{\partial y} = \rho \frac{\partial v_x}{\partial t} & \text{momentum} \\ \rho C_V \frac{\partial \theta}{\partial t} = \kappa \frac{\partial^2 \theta}{\partial y^2} + \beta \tau \frac{\partial v_x}{\partial y} & \text{energy} \\ \frac{\partial \gamma}{\partial t} = \frac{\partial}{\partial t}\left(\frac{\partial u_x}{\partial y}\right) = \frac{\partial v_x}{\partial y} & \text{geometry} \\ \tau = f(\gamma, \dot{\gamma}, \theta) & \text{constitutive} \end{cases}. \tag{15}$$

To eliminate the stress, τ, the constitutive equation in system (15) can be rewritten as a stress gradient pattern by the chain rule:

$$\frac{\partial \tau}{\partial y} = P\frac{\partial \gamma}{\partial y} + Q\frac{\partial \dot{\gamma}}{\partial y} + R\frac{\partial \theta}{\partial y}, \tag{16}$$

where P, Q, and R are defined as

$$P \overset{\text{def}}{=} \left(\frac{\partial \tau}{\partial \gamma}\right)_{\dot{\gamma},\theta},$$

$$Q \overset{\text{def}}{=} \left(\frac{\partial \tau}{\partial \dot{\gamma}}\right)_{\gamma,\theta},$$

$$R \overset{\text{def}}{=} \left(\frac{\partial \tau}{\partial \theta}\right)_{\gamma,\dot{\gamma}}.$$

The solution of system (15) can be assumed in vector form: $\mathbf{v} = [\gamma\, v_x\, \theta\, \eta]^{\mathrm{T}}$, where $\eta = \partial\theta/\partial y$. Based on the strain rate distribution in ASB [74], the strain rate along the y direction can be approximated as constant. Thus, the term containing Q in equation (16) is zero and can be eliminated. By substituting equation (16) into the momentum equation in system (15), the system can be linearized in matrix form, as follows:

$$\begin{bmatrix} 1 & 0 & 0 & 0 \\ 0 & 1 & 0 & 0 \\ 0 & 0 & 1 & 0 \\ 0 & 0 & 0 & 0 \end{bmatrix} \frac{\partial \mathbf{v}}{\partial t} + \begin{bmatrix} 0 & -1 & 0 & 0 \\ -\frac{P}{\rho} & 0 & -\frac{R}{\rho} & 0 \\ 0 & -\frac{\beta\tau}{\rho C_V} & 0 & -\frac{\kappa}{\rho C_V} \\ 0 & 0 & 1 & 0 \end{bmatrix} \times \frac{\partial \mathbf{v}}{\partial y} = \begin{bmatrix} 0 & 0 & 0 & 0 \\ 0 & 0 & 0 & 0 \\ 0 & 0 & 0 & 0 \\ 0 & 0 & 0 & 1 \end{bmatrix} \mathbf{v}. \tag{17}$$

For the three matrices in equation (17), $\mathbf{M}_1$, $\mathbf{M}_2$, and $\mathbf{M}_3$ are assigned as references. They are given by

$$\mathbf{M}_1 = \begin{bmatrix} 1 & 0 & 0 & 0 \\ 0 & 1 & 0 & 0 \\ 0 & 0 & 1 & 0 \\ 0 & 0 & 0 & 0 \end{bmatrix},$$

$$\mathbf{M}_2 = \begin{bmatrix} 0 & -1 & 0 & 0 \\ -\frac{P}{\rho} & 0 & -\frac{R}{\rho} & 0 \\ 0 & -\frac{\beta\tau}{\rho C_\mathrm{V}} & 0 & -\frac{\kappa}{\rho C_\mathrm{V}} \\ 0 & 0 & 1 & 0 \end{bmatrix},$$

$$\mathbf{M}_3 = \begin{bmatrix} 0 & 0 & 0 & 0 \\ 0 & 0 & 0 & 0 \\ 0 & 0 & 0 & 0 \\ 0 & 0 & 0 & 1 \end{bmatrix}.$$

The solution, $\mathbf{v}$, in a general form can be given by the superposition of an exact solution and a perturbation, as follows:

$$\mathbf{v} = \mathbf{v}_{0(t,y)} + \mathbf{v}_1 e^{\alpha t + iky}, \tag{18}$$

where $\mathbf{v}_{0(t,y)}$ is the exact solution of system (17); $\mathbf{v}_1 e^{\alpha t+iky}$ is the perturbation; $\mathbf{v}_1$ is a constant; α is the perturbation decay; and k is the wave number. Because the solution, $\mathbf{v}$, and exact solution, $\mathbf{v}_{0(t,y)}$, must satisfy system (17), the perturbation part must also satisfy this system. The perturbation equation is given by

$$\mathbf{M}_1\mathbf{v}_1\frac{\partial\left(e^{\alpha t+iky}\right)}{\partial t} + \mathbf{M}_2\mathbf{v}_1\frac{\partial\left(e^{\alpha t+iky}\right)}{\partial y} = \mathbf{M}_3\mathbf{v}_1\left(e^{\alpha t+iky}\right). \tag{19}$$

Equation (19) can be rearranged into one term as

$$\mathbf{M}\mathbf{v}_1 = 0, \tag{20}$$

where

$$\mathbf{M} = \begin{bmatrix} \alpha & -ki & 0 & 0 \\ -\frac{Pki}{\rho} & \alpha & -\frac{Rki}{\rho} & 0 \\ 0 & -\frac{\beta\tau ki}{\rho C_\mathrm{V}} & \alpha & -\frac{\kappa ki}{\rho C_\mathrm{V}} \\ 0 & 0 & ki & -1 \end{bmatrix}.$$

Equation (20) requires that the determinant be zero to guarantee that $\mathbf{v}_1$ is not trivial. Consequently, a spectral equation is obtained by solving $\det(\mathbf{M}) = 0$ in polynomial form as follows,

$$C_\mathrm{V}\alpha^3\rho^2 + C_\mathrm{V}\alpha^2k^2\kappa\rho^2 + C_\mathrm{V}P\alpha k^2\rho + R\alpha\beta k^2\tau + C_\mathrm{V}Pk^4\kappa\rho = 0. \tag{21}$$

The solution of equation (21) is given by

$$\alpha = -\frac{C_\mathrm{V}P\rho + R\beta\tau}{2C_\mathrm{V}\kappa\rho^2}\left[1 \mp \sqrt{1 - \frac{4C_\mathrm{V}Pk^2\kappa^2\rho^3}{(C_\mathrm{V}P\rho + R\beta\tau)^2}}\right]. \tag{22}$$

By assuming that $k^2 \to \infty$, the square root term in equation (22) becomes an imaginary number and is thus neglected. Subsequently, system stability is only determined by the real part,

$$\mathrm{Re}(\alpha) = -\frac{C_\mathrm{V}P\rho + R\beta\tau}{2C_\mathrm{V}\kappa\rho^2}. \tag{23}$$

Substitute the definitions of P and R into equation (23). The perturbation amplification requires $\mathrm{Re}(\alpha) > 0$. Then, the unstable domain of the system is reached by satisfying an unequal relationship,

$$\text{Criterion 2}: \frac{\partial\tau}{\partial\gamma} < \frac{-\beta\tau\frac{\partial\tau}{\partial\theta}}{C_\mathrm{V}\rho}. \tag{24}$$

In Criterion 2, the right-hand side is consistently positive because $\partial\tau/\partial\theta$ must be a negative number for typical ductile materials. Thus, Criterion 2, given by the perturbation method, is less stringent than Criterion 1 that requires $\partial\tau/\partial\gamma$ to be less than zero. Criterion 2 is consistent with Bai's criterion [14]. Notably, Criterion 2 does not explicitly include the contribution of the strain rate. However, the strain rate does affect the ASB onset. In 1982, Bai [14] provided an additional criterion involving strain rate. The extra criterion is in terms of the characteristic time,

$$t_\mathrm{C} \geqslant \frac{Q^*}{\dot{\gamma}}\frac{\rho C_\mathrm{V}}{\beta\tau R - \rho C_\mathrm{V}P}, \tag{25}$$

where t_C is the characteristic time comparable to the ASB onset time, and Q^* is the current strain rate hardening. Inequality (25) indicates that the ASB onset must be completed within t_C, which is a relative value. Therefore, the strain rate, $\dot{\gamma}$, is required by the ASB onset to be on the right side of inequality (25); it must be sufficiently high to ensure that the right side is less than the characteristic time.

In 1962, Recht proposed a simple criterion [15] derived from a constitutive equation in a general form. The criterion, which neglects the strain rate is, defined as $\tau(\gamma, \theta(\gamma))$. The derivative of the general constitutive equation is given by

$$\frac{d\tau}{d\gamma} = \frac{\partial\tau}{\partial\gamma} + \frac{\partial\tau}{\partial\theta}\frac{d\theta}{d\gamma}. \tag{26}$$

Based on the criterion 1, the criterion can be expressed as

$$\text{Criterion 3}: 0 \leqslant \frac{\partial\tau/\partial\gamma}{(-\partial\tau/\partial\theta)(d\theta/d\gamma)} \leqslant 1. \tag{27}$$

Criterion 3 depicts the competition between thermal softening and strain hardening. Nevertheless, the fundamental principle of this equation is originally based on engineering experience. In particular, material instability occurs when the stress–strain curve exhibits a negative slope because material softening overcomes material hardening. Therefore, Criterion 3 is more of an engineering standard rather than a scientific rule. Another drawback is that temperature is typically determined not only by strain. In Criterion 3, temperature is considered a function of strain, but in other criteria temperature is usually treated as an independent variable.

In 2014, Cai and Dai [10] built an ASB onset system for constraint cutting in which the compressions from the cutter tip and the constraint were considered. The criterion is given by

$$\text{Criterion 4}: Cr_4 = \frac{B}{1+N+2\sqrt{A\,(M+CN)}} > 1, \tag{28}$$

where N, M, A, B, and C are dimensionless numbers constructed by material properties and mechanical quantities. In 2018, a criterion involving cutter compression and material convection effect was established by Ye *et al* [16]. In their study, Bai's criterion is modified as follows,

$$\text{Criterion 5}: Cr_3 = \frac{1}{1+{P_r}^{-1/2}\Pi - Da} Cr_1 > 1, \tag{29}$$

where P_r is the Prandtl number (ratio of viscous diffusion velocity to thermal diffusion velocity); Π is the tool compression coefficient; and Da is the effective damage number proposed by Johnson [75]. In Criterion 5, the contribution of strain rate hardening is implicitly included in P_r and Π. Generally, Criteria 4 and 5 can similarly depict the ASB onset in the PSZ.

All these criteria pertain to the timing of the ASB onset with increasing loading rate. However, the ASB onset cannot occur when the loading rate is sufficiently high to cause shock. In the future, the criteria for assessing the ASB onset transiting to shock needs to be established.

2.1.5. Failure models of ASB. The failure of ASBs is dominated by microscopic void nucleation, growth, and coalescence. As shown in figure 4(a), during the ASB formation process, stress initially increases with void nucleation. When the stress reaches the summit of the curve, the material between the two adjacent voids also reaches the ultimate stress. With the further growth of the ASB, the materials surrounded by voids start to neck, and the voids continuously grow in size. These voids coalesce to form complete cracks, resulting in the complete material failure. These voids evolution can be identified in figure 4(b). Several failure models have been proposed to describe the process. Different from conventional stress-based or strain-based models, failure models examine the void volume fraction in materials to assess failure. The void volume fraction is given by $D = V_{\text{void}}/(V_{\text{void}} + V_{\text{solid}})$, where V_{void} and V_{solid} are the void and solid volume parts in unit volume. The concept of 'unit volume' is different from its conventional meaning. This volume must be sufficiently large to indicate the void volume fraction at the macroscale and sufficiently small to represent a unit. Gao and Zhang [23] first proposed this concept in 1977. In his work, two types of unit volumes with different shapes were assumed: cylinders and spheres. Based on assuming a unit volume, the void fraction volume can be included in the yield surface equation by equating the plastic work at the mesoscale and macroscale. Although the failure criterion was not explicitly expressed in Gurson's model, the study provided enlightenment to subsequent research.

Seaman *et al* [25] conducted shocking experiments and counted the number of voids in aluminum 1145. They found that the number of voids followed a negative exponential distribution with respect to the void radius:

$$N = N_0 \exp\left(-\frac{R}{R_1}\right), \tag{30}$$

where R_1 is a distribution parameter; R is the void radius; N_0 is the total number of voids; and N is the number of voids whose radii are greater than R. Based on this statistical distribution, the total volume of the voids in the unit cube can be obtained by integration over the entire distribution:

$$V_{\text{void}} = \int_0^{+\infty} \frac{4\pi}{3} R^3 \mathrm{d}N = \int_0^{+\infty} \frac{4\pi}{3} R^3 \frac{\mathrm{d}N}{\mathrm{d}R} \mathrm{d}R. \tag{31}$$

By differentiating equation (30) with respect to R and substituting equation (31), the total void volume can be expressed as

$$V_{\text{void}} = 8\pi N_0 R_1^3. \tag{32}$$

The total volume of voids is derived from two sources: void nucleation and growth. Assume that the void volume contributed by the two sources obeys equation (32). The volume increase rate can then be expressed in a discrete time manner:

$$\begin{aligned}\Delta V_{\text{void}} = \Delta V_n + \Delta V_g = 8\pi \dot{N}_{n0} e^{[P_S - P_{n0}]/P_1} R_n^3 \Delta t \\ + 8\pi N_0 R_{10}^3 e^{3[P_S - P_{n0}]\Delta t/(4\eta)}.\end{aligned} \tag{33}$$

Because the volume fraction, D, is defined by V_{void}, equation (33) can be used to calculate the critical volume fraction, D_{cr}, for assessing material failure. All the variables with the subscript '0' denote the variables at the beginning of the time interval.

In 1984, Tvergaard and Needleman [26] developed a model modified from Gurson's model [24] by redefining the microstructural evolution as

$$F = \left(\frac{\sum_{\text{eqv}}}{\sigma_Y}\right)^2 - 2D^* q_1 \cosh\left(\frac{\sum_{kk}}{2\sigma_Y}\right) - 1 - q_3 D^{*2}, \tag{34}$$

where D^* is a function of volume fraction D. Moreover, D^* can be expressed by

$$D^* = \begin{cases} D & D \leqslant D_{\text{cr}} \\ D_{\text{cr}} + \frac{D_u^* - D_{\text{cr}}}{D_F - D_{\text{cr}}}(D - D_{\text{cr}}) & D > D_{\text{cr}} \end{cases},$$

where D_{cr} is the volume fraction at the void coalescence stage; D_F is the volume fraction at the material fracture stage; and D_u^* is equal to $1/q_1$. This model (also called the Gurson–Tvergaard–Needleman model) offers an improved way to describe the void volume fraction because the void shape changes significantly after coalescence.

In 1986, Perzyna [76] estimated the evolution of void volume depending on stress, strain, and thermal activation. In 2001, Tonks *et al* [77] proposed a void volume fraction model based on the impact testing of a uranium alloy. Generally, these models based on void volume fraction provide a more realistic description of the void volume evolution.

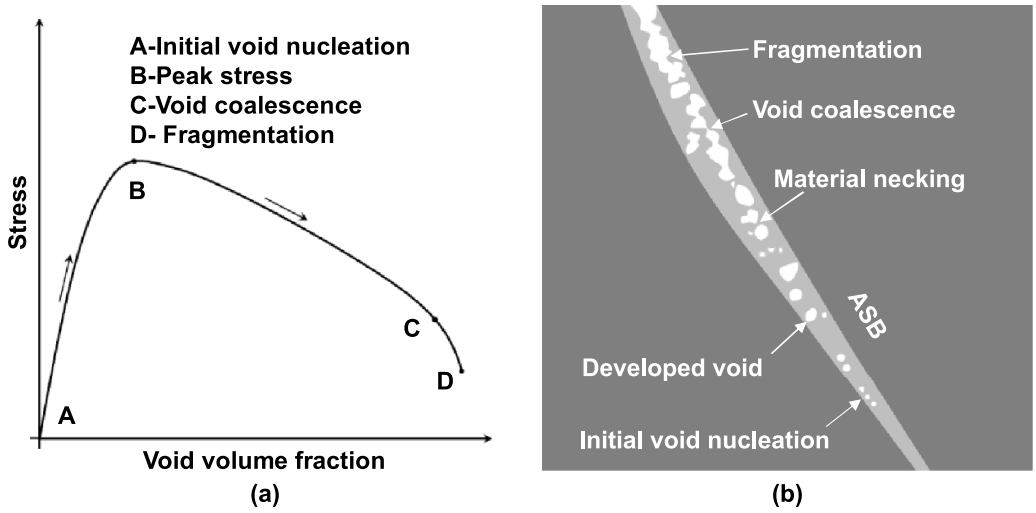

Figure 4. Micro-void evolution influence curve of stress versus void volume fraction: (a) curve of stress versus void volume fraction and (b) stages of micro-void evolution [36, 86].

In recent decades, researchers have studied the underlying mechanism of void evolution at the atomic scale. To determine this mechanism, at least two questions must be answered. The first question is, how do voids nucleate? To answer this, void nucleation is classified into two categories [78]. In the first category, voids preferentially nucleate at interfaces, such as grain boundaries and interfaces among different phases [79]. Before voids nucleate, microcracks nucleate owing to local stress. As the local stress around the cracks increases, local plastic deformation drives microcracks to transition to micro-voids. In the second category, voids may nucleate from dislocation networks and vacancies. In 1995, Cuitino and Ortiz [80] built a void nucleation model based on dislocation jog and pipe diffusion. However, the time for a void to nucleate must be in the order of 1 min, which is extremely long for dynamic activities and inconsistent with the characteristic time of ASB formation. In 2011, Reina *et al* [81] discarded the assumption that voids are generated by dislocation jogging. Instead, the equilibrium void concentration is assumed to correlate with temperature and volumetric deformation. Based on this assumption and the Monte Carlo simulation approach, void nucleation was verified to be caused by the aggregation of vacancies and cavity clusters. In their study, strain rate, temperature, and hydrostatic stress were considered. The results show that the void nucleation time is in the order of 10^{-9} s.

The second question regarding void evolution is what contributes to void growth? In 1960, Rice and Tracey [33] proposed a relationship in which void growth is controlled by the strain rate around an isolated void and hydrostatic stress. This relationship was modified by Huang in 1991 [34] based on the Rayleigh–Ritz method. Johnson and Cook [69] proposed a criterion based on stress triaxiality for assessing ductile material failure; hydrostatic stress was the dominant factor in the criterion. To study the underlying mechanism of micro-void growth further, numerous subsequent studies utilized large-scale MD that could improve characterizations for simulating the void evolution process. Seppala *et al* [28, 29, 82] simulated the void growth in the single-crystalline copper at high strain rates and observed that dislocations grew around the voids. Marian *et al* [83, 84] studied single-crystalline aluminum and found that pre-existing voids grew by emitting dislocations that multiplied to form loops and junctions. In 2008, the same phenomenon was observed in copper and aluminum [31, 85]. Nevertheless, Nguyen and Warner [32] discovered that the time for dislocation nucleation was unreasonably long based on the results of MD simulations and transition state theory calculations. In 2020, based on the findings of Nguyen and Warner, Sills and Boyce [30] proposed a mechanism that attributed void growth to the dislocation-adsorption mechanism. Therefore, a discrepancy is apparent; both the hydrostatic stress and dislocation multiplication trigger dislocation growth because dislocation multiplication is driven by shear stress. This discrepancy can be explained by the scale effect. This means that hydrostatic stress works at the macroscale but in a local site, and the resolved stress drives dislocation multiplication to expand voids.

Thus far, the mechanism for void nucleation and growth has been studied based on simulations and theoretical calculations; however, conclusive experimental evidence is insufficient. In the future, more experimental observations are required to elucidate the underlying mechanisms.

2.2. *Solid mechanics description of shock*

2.2.1. Transition from ASB to shock. Studies on ASB in the PSZ have lasted for several decades. Previous studies have mainly focused on the ASB formation with increasing machining speeds. In 2013, Monilari *et al* [55] reported the depression of ASB with increasing machining speed. Based on the results of the MD simulation we conducted, the ASB is depressed because of the increase in hydrostatic stress caused by the shock in UHSM.

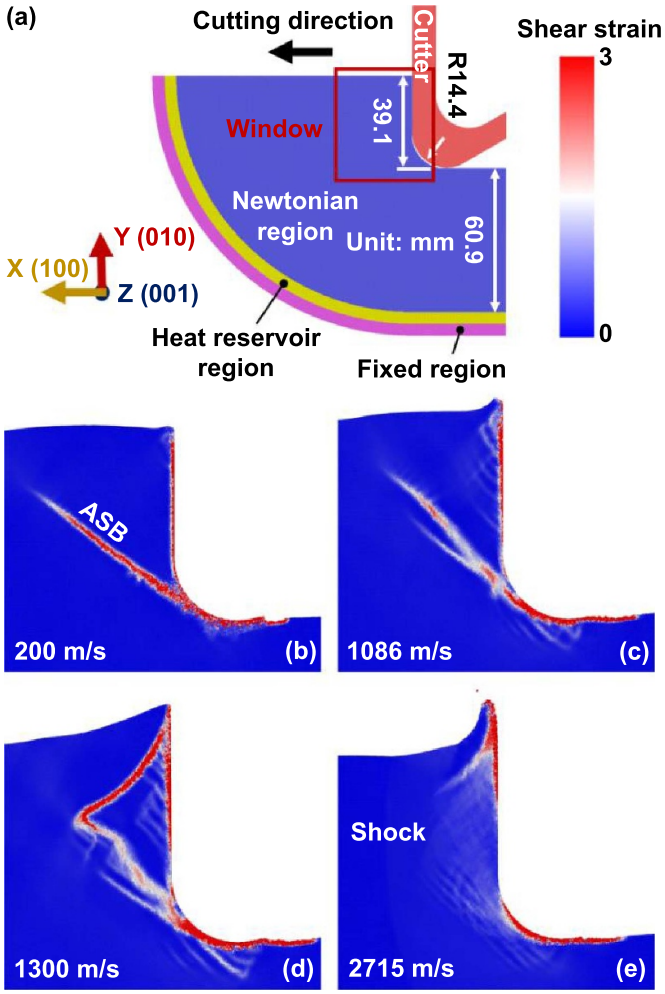

Figure 5. Evolution of ASB in single-crystal silicon machined at various cutting speeds simulated by LAMMPS: (a) configuration of simulation and (b)–(e) morphs of ASB at various cutting speeds.

The MD simulation configuration of UHSM is shown in figure 5(a). As shown in figure 5(a), a single-crystal silicon model was machined using a diamond cutter along [100] direction with an uncut thickness of 39.1 nm. The thickness of the model is 1.5 nm. The cutter moved at a speed ranging 200–2715 m s^{-1}; cutting was operated at room temperature. A window was set in front of the cutter to observe the microstructural evolution during cutting. The shear strain field is used to indicate the ASB, as shown in figures 5(b)–(d). This MD simulation was conducted using a large-scale atomic/molecular massive parallel simulator.

The diamond cutter was assumed as a perfectly rigid body. Three type atoms were set for the workpiece. Newtonian atoms were used for the interaction among single-crystalline silicon; heat reservoir is used for model temperature balance; the fix boundaries were set as figure 5(a). The potential function used in this simulation is the modified Tersoff function [87] that has been validated by the shock experiments [88] and the first-principle calculation [87].

The distinct failure modes in front of the cutter with increasing machining speed are shown in figures 5(b)–(d). As shown in figure 5(b), the main ASB onset originates from a location beneath the cutter nose and extends to the free surface at an angle of approximate 52°. Most plastic deformation occurs within the ASB, resulting in extremely heterogeneous deformation. As shown in figure 5(c), when the machining speed is 1086 m s^{-1}, the ASB becomes wavy. The subsidiary branch deviates from the extending direction of the main ASB, forming a bifurcation. The local maximum shear stress and corresponding direction may be responsible for the ASB bifurcation. Additionally, many micro-ASBs grow from the interface between the cutter and material. A similar phenomenon regarding temperature turbulence was reported by Teng *et al* in 2007 [89]. In figure 5(d), the main ASB originates from the upper-right corner and extends to join the main ASB. Compared with the case in which the speed is 1086 m s^{-1}, the main ASB at the lower location becomes wavier. Further, more micro-ASBs grow from the material-cutter interface. In figure 5(e), when the cutting speed is increased to 2715 m s^{-1}, the main ASB is eliminated, and more micro-ASBs occur. These micro-ASBs are immature and cross each other to form ASB nets. This damage in a net pattern is a prominent feature of shock damage. By examining the cases in figures 5(b)–(e), the failure mode transits from extremely heterogeneous deformation caused by the ASB to homogeneous deformation caused by shock damage. The material failure transition also represents the stress-type dominant material behavior transition from shear stress to hydrostatic stress [18, 90].

2.2.2. Shock wave in UHSM. The shock in UHSM has not received sufficient research attention; nevertheless, UHSM can be considered as a special impact process. This lack of attention is probably because the machining speed in an experiment cannot reach the speed that causes shock. Based on our simulations, shock occurs at a machining speed exceeding 2700 m s^{-1} for the single-crystalline silicon. In contrast, in the Molinari simulation [55], ASBs are depressed at a machining speed of 350 m s^{-1} for titanium alloys. This machining speed is already extremely high for most experiments. To build a complete theoretical framework for UHSM, this section reviews the fundamental theorem for shock in UHSM.

In UHSM, a shock wave is formed by the impact of a cutter, as shown in figure 6(a). In figures 6(a) and (b), one shock wave is emitted from the interface between the workpiece and cutter. It is led by the shock front, which has extremely high hydrostatic stress. As the shock wave propagates, its energy is consumed by the material through which it passes; it dissipates in the form of plastic deformation. Therefore, the shock wave continuously attenuates as it propagates; This attenuation is described in figure 6(b). In figure 6(b), the horizontal axis is the x axis of the Euler coordinates defined in figure 6(a), and the vertical axis represents the hydrostatic stress at the shock front. The shock wave decay and attenuation take place during the time t_1–t_4 and cease when a steady state is reached, which is rendered by the time t_4 and t_5 in figure 6(b). At the steady state, the shock wavelength remains constant.

Notably, the stress state for an arbitrarily selected material point varies from a free state to an extremely high stress

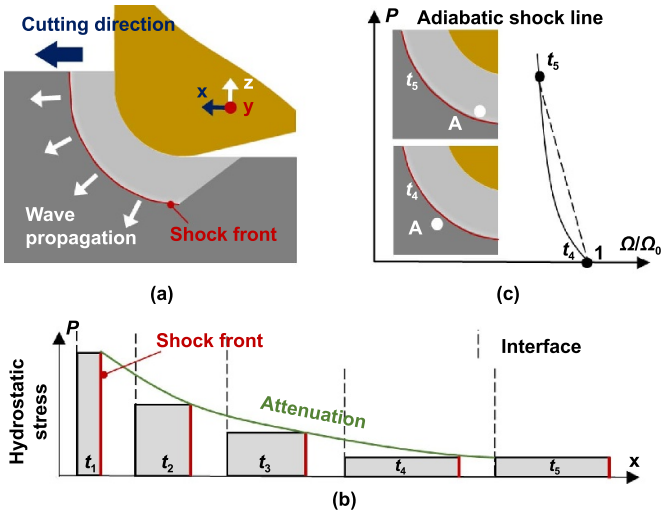

Figure 6. Shock wave evolution and stress jump from free state to extremely high-stress state in UHSM. (a) Shock wave profile is caused by impacting of cutter. (b) Shock wave decays and attenuates from t_1 to t_5. The time t_4 and t_5 represents the steady state is reached. (c) Point A jumps to extremely high stress state from free state over extremely short time $(t_5 - t_4)$.

state over an extremely short period. In figure 6(c), the time required for the arbitrary material point, A, to jump to an extremely high-stress state is extremely short such that the process must be treated as discontinuous. The mechanical description of the discontinuous process is based on state variables. As shown in figure 6(c), point A is initially free at time t_4, implying that no volume compression exists for point A at time t_4. Once the shock front passes point A, the corresponding time is denoted as t_5, and the stress directly jumps to an extremely high level. Because the process from time t_4 to t_5 is discontinuous, the conservation equations can link the physical quantities at the states corresponding to t_4 and t_5. The three conservation equations are

$$\begin{cases} \rho_0 v_S = \rho (v_S - v_P) & \text{Mass conservation} \\ (P - P_0) = \rho_0 v_S v_P & \text{Momentum conservation} \\ E - E_0 = \frac{1}{2}(P + P_0)(\Omega_0 - \Omega) & \text{Energy conservation} \end{cases}, \tag{35}$$

where ρ_0 is the material density at the initial stage; Ω_0 is the specific volume at the initial stage (equal to $1/\rho_0$); ρ is the material density at the high-pressure stage; Ω is the specific volume at the high-pressure stage (equal to $1/\rho$); P_0 is the pressure at the initial stage; P is the pressure at the high-pressure stage; v_S is the velocity of the shock wave; v_P is the velocity of the material particles; E_0 is the internal energy at the initial stage; and E is the internal energy at the high-pressure stage. The three equations in system (35) are conventionally called Rankine–Hugoniot jump conditions to commemorate the studies of Rankine and Hugoniot [91]. By combining the mass and momentum conservation equations in system (35), the shock wave speed can be given in terms of hydrostatic stress and specific volume:

$$v_S = \sqrt{\frac{1}{\rho_0} \frac{P - P_0}{(1 - \Omega/\Omega_0)}}. \tag{36}$$

The second term in the square root of equation (36) is the volumetric modulus; it can be expressed as the slope of the line connecting initial and end state shown in figure 6(c).

In UHSM, the material volumetric compression caused by the cutter can be simply evaluated through conservation equations and an extra equation of state (EOS). For a simple microstructural evolution, the EOS can be expressed in a simple form [17]:

$$v_s = C_0 + S_1 v_p \tag{37}$$

where C_0 is the speed of sound in the material without pressure, and S_1 is a material parameter. If phase transformation or other complex metallurgical evolution is involved, the EOS must be given by the Mie–Grüneisen form [92]:

$$P - P_{0K} = \frac{\gamma}{\Omega}(E - E_{0K}), \tag{38}$$

where P_{0K} is the pressure in the material at 0 K; E_{0K} is the internal energy at 0 K; and γ is the Grüneisen constant. The theoretical frame constructed by the Rankine–Hugoniot jump condition and EOS can provide a complete description of the shock. Moreover, it can be involved in standard numerical simulations [93].

3. Material microstructural evolution

3.1. Material deformation history in HSM

The plastic flow in front of the cutter can be divided into two streams. The upper stream flows upward to form chips, and the lower stream flows down to form a new surface and a part of the subsurface. Because the upper and lower streams flow along different paths, the plastic deformations in the two streams differ.

To demonstrate this, the general stress state beneath a cutter is analyzed, as shown in figure 1. In figure 7, a stagnation region is assumed because it can occur in the HSM. The machining process is decomposed into two actions: vertical and horizontal. The two actions induce distinct stress states in the subsurface of the workpiece. For the stress state caused by vertical compression, the compressive stress ($\mathbf{P}_{comp}$) along the vertical direction dominates the stress state in the central region beneath the cutter, and the shear stress ($\mathbf{S}_{comp}$) is located in the side region beneath the cutter. For cutter sliding-induced stress, a more complex stress distribution occurs. As shown in figure 7(b), the stagnation region divides the uncut materials into two material streams. The upper material stream flows toward the cutter rake face, forming chips. In the chip formation process, the material forming chipping experiences severe shear stress ($\mathbf{S}_{Chipping}$), resulting in severe strains of up to several hundreds of percent based on the Piispanen card model [1]. The lower material stream flows under the cutter nose and bears higher compression. In this process, the compressive stress ($\mathbf{P}_{sliding}$) and shear stress ($\mathbf{S}_{sliding}$) are caused

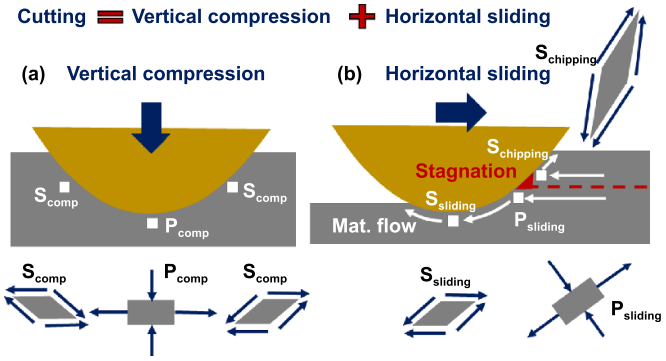

Figure 7. General form of stress superposition in cutting: (a) stress distribution caused by vertical compression and (b) stress distribution caused by the horizontal sliding.

by the cutter sliding. In cutting, the stress below the stagnation region is superposed by the stress respectively caused by compression and sliding, affecting the damage to the top layer of the subsurface. The stress exceeding the stagnation region governs the formation of chips. Therefore, the material that forms chips and causes subsurface damage experience distinct deformation, further resulting in distinct extents of failure. The material microstructural evolution in chips and subsurface are reviewed in sections 3.2 and 3.3, respectively.

3.2. Material microstructural evolution in ASBs of chips

In HSM, the chip morphology evolves into continuous, serrated, and fragmented chips with increasing machining speed. The most severe deformation occurs in the ASBs of serrated and fragmented chips [94–96], causing various microstructural evolutions. The degree of plastic deformation in continuous chips is typically lower than that in ASBs. Accordingly, this section focuses on the microstructural evolution of the ASBs in ductile materials.

The formation of ASBs is a process associated with thermomechanical coupling. This thermal effect causes the temperature at the center of the ASB to be higher than the temperature at the two ASB edges. In 1996, Zhou *et al* determined the temperature and its distribution within an ASB in a Ti6Al4V material [97]. They found that the maximum temperature at the center of the ASB may even reach the material melting point under high-strain-rate loading [98, 99]. Therefore, the microstructural evolution at the center of the ASB is distinct from that at its two edges. For most ductile materials (including body-centered crystalline (BCC) [100, 101], face-centered crystalline (FCC) [102, 103], and hexagonal close-packed [104, 105] alloys), EFGs are the main microstructures at the center of the ASB. In contrast, at the two edges, elongated grains are the main microstructures [38, 106]. The EFGs at the center are typically considered to be the result of DRX, which is one of the most significant microstructural evolutions in ASBs.

The main underlying mechanism of the evolution of large grains in the ASB to EFGs is DRX. Previous studies have generally classified DRX into three categories [107]: continuous

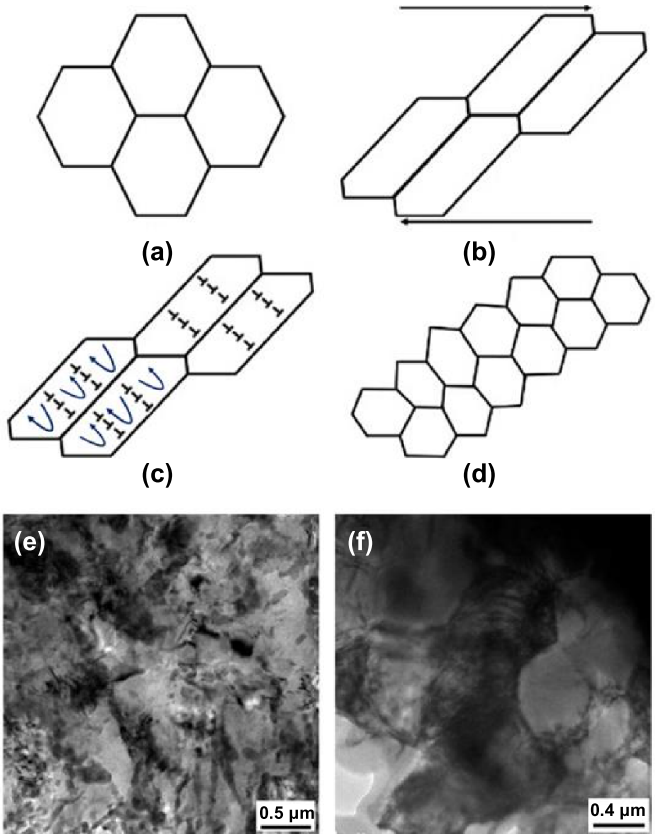

Figure 8. Rotation mechanism of EFG formation: (a)–(d) CDRX process within ASB (Reprinted from [114], Copyright (2017), with permission from Elsevier); (e) grain structure at transitional zone near center of ASB ; and (f) EFGs at center of ASB in AISI 1045 steel (Reprinted from [38], Copyright (2012), with permission from Elsevier).

DRX (CDRX), discontinuous DRX, and geographic DRX. Specifically, the EFGs in ASBs are presumed to result from the CDRX; this is because of at least two reasons. First, the temperature within the ASB can reach a range exceeding $0.5T_m$, where T_m is the melting point. This temperature is necessary to process the CDRX. Second, based on the characterization of EFGs in ASBs, the grain sizes are homogeneous; the homogeneity of grain size is a key feature of CDRX [107]. A typical CDRX within the ASB is illustrated in figures 8(a)–(d). Initially, the original grains exhibit an equiaxed shape, as shown in figure 8(a). The grains are then elongated and driven by shear stress, as illustrated in figure 8(b). In figure 8(c), as the shear strain increases, dislocations accumulate to form low-angle grain boundaries (LAGBs). The EFGs shown in figure 8(d) are formed by rotating the EFGs of the LAGBs shown in figure 8(c) [108]. Owing to the EFG rotations, the grain misorientations in figure 8(d) are higher than those shown in figure 8(c). Based on the post-mortem characterization shown in figure 8(f), the dislocation densities in the EFGs are lower than those in the original grains, and the grain size of the EGFs is less than 1 μm. The underlying mechanism of dislocation density decrease is that the original dislocations were released by forming more grain boundaries [107]; This mechanism also causes EFGs. The underlying mechanism of

the EFG formation may be also related to the high cooling rate within the ASB after it is formed [99], leaving the grains with insufficient time for growth.

An argument on whether phase transformation occurs in CDRX was raised. It originates from the fact that two types of ASB may exist in ferrous metals: grain deformation-formed ASB and transformed ASB. The latter is also called the white-etched band because it is white and has boundaries distinct from the surrounding materials when viewed under an optical microscope. The transformed band is presumed to include EFGs induced by phase transformation [36]. However, this viewpoint is challenged by the opinion that DRX is the main contributor to the formation of EFGs [109]. In this study, only two microstructures are characterized within the ASB of the AISI 304 L material; Duan and Zhang [38] and Velasquez *et al* [110] have drawn similar conclusions for the AISI 1045 steel and Ti6Al4V titanium alloy, respectively. In contrast, martensitic phase transformation has been identified in a type of armor steel [111] and 30CrNiMoV low-alloy steel [112]. This discrepancy may have arisen due to differences in loading rate and material. Higher loading rate causes higher temperature gradient across ASBs. The higher temperature at the center of the ASBs provides an environment for some materials to transform phase. However, for the other materials, phase transformation cannot occur. Therefore, when loading rate is sufficiently high, EFGs occur in most materials, but phase transformation occurs in part of materials. Further discussion on phase transformation in ASBs is found in the review of Xu *et al* [113].

3.3. Material microstructural evolution in subsurface

Based on the analysis presented in section 3.1, the stress state of the subsurface under the cutter nose is complex and superposed by compressive hydrostatic and shear stresses. Because the machining speed in HSM is high, the complex dynamic stress causes rapid heating and cooling at the subsurface. The rapid heating and complex stress in machining cause DRX, and the rapid cooling after machining influences the continuous growth of EFGs at the subsurface.

In the manufacturing industry, the layer of EFGs at the subsurface is conventionally called the white layer (WL) because it exhibits a white color under an optical microscope. Similar to the classification in ASBs, the WL can also be classified as a mechanically induced WL (M-WL) at a relatively low machining speed and a thermally induced WL (T-WL) [35] at a relatively high machining speed. This similarity may originate from the fact that both the ASB and WL are material responses to the combination of high stress and temperature. This section reviews the phase transformation of WLs during HSM. Subsequently, the WL depth and damage to the subsurface of the brittle material during HSM are discussed.

For decades, the phase transformation in the WL of ferrous and nonferrous metals has been investigated. In 1999, Chou and Evans [45] proposed that austenitic transformation could occur in the WL of ferrous metals. This was because FCC(γ) austenite was the major component of the WL after the hard turning of VIMVAR 52100 steel. In 2005, Ramesh *et al* analyzed the WL in an AISI 52100 steel manufactured by hard turning [46]. The orthorhombic-(θ) cementite clusters in the WL were eliminated at a machining speed of 4.5 m s^{-1}, implying that carbon was dissolved. The dissolution of carbon may imply that rapid heating causes austenitic phase transformation ($\alpha \rightarrow \gamma$). In 2012, Hosseini *et al* [115] proposed a similar viewpoint. Subsequently, Hosseini *et al* [35] analyzed the components of the WL of the AISI 52100 steel: BCC-(α) ferrite and orthorhombic-(θ) cementite were the major components of M-WL; FCC(γ) austenite, BCC(α) martensite, and orthorhombic(θ) cementite were the major components of T-WL. The occurrence of FCC(γ) austenite in T-WL may be related to the phase transformation ($\alpha \rightarrow \gamma$) during relatively highspeed turning.

The phase transformation in the T-WL of nonferrous metals (including nickel-based and titanium alloys) was investigated. Österle and Li [116] discovered the dissolution of phase-γ' in Ni-based alloys. In 2019, Liao *et al* [117] characterized a nickel-based superalloy (S135H) by transmission electron microscopy and transmission Kikuchi diffraction. The characterization of phase-γ' dissolution with depth in the WL is shown in figure 9. The dissolution of phase-γ' and the corresponding local temperature are presented in figure 9(a), and the metallurgical microstructure is illustrated in figure 9(b). The WL depth measured from the free surface was 8 μm. As shown in figure 9, both the temperature and strain rate gradients sharply increased at a depth of 2 μm. The temperature at this depth causes substantial phase-γ' dissolution and the occurrence of EFGs. When the depth is 2–4 μm, phase-γ' dissolution is alleviated because of the low local temperature and existence of large grains resulting from dynamic recovery (DRV). At deeper locations, stress dominates the plastic deformation at lower temperatures, causing phase-γ' to be separated by dislocation arrays. At a depth of 2 μm, figure 9 clearly shows that DRX is associated with the transformation from phase-γ' to phase-γ through dissolution, verifying the occurrence of phase transformation. For titanium alloys, whether or not phase transformation occurs in the WL remains controversial. Velásquez *et al* [110, 118] claimed that no phase transformation occurs in the WL of Ti6Al4V at machining speeds of up to 11 m s^{-1}. Nevertheless, in 2019, Xu *et al* [119] discovered that phase-α transforms into phase-β in the WL at a machining speed of 4.25 m s^{-1}. Based on the characterization by precession electron diffraction, the precipitation of phase-β from phase-α in the WL was observed. Thus far, insufficient evidence has been presented to support the occurrence of transformation from phase-α to phase-β. Therefore, more specific investigations on the phase transformation of the WL in titanium alloys must be conducted in the future.

The EFGs created in the WL are detrimental to the performance of workpieces. For instance, in ferrous metals, the WL is a hard and brittle material associated with residual stress [46, 120]. In nonferrous metals, such as nickel-based alloys, the supersaturation of phase γ diminishes the yield strength of the WL [117], and the lifetime of workpieces subjected to low-cycle fatigue tests is significantly reduced [121]. Nevertheless, the WL depth decreases with machining speed (figure 10), as reported by Bosheh and Mativenga [120]. As shown in figure 10(a), the WL depth in the H13 tool steel was 2.3 μm

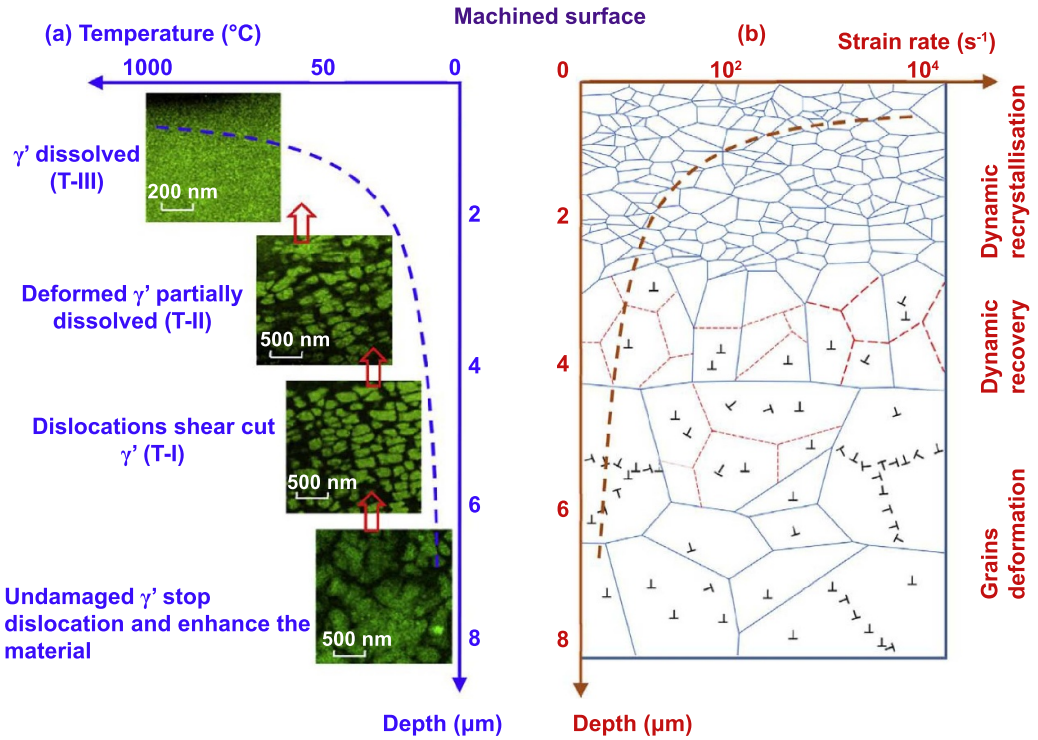

Figure 9. Variation in phase-γ' dissolution and microstructural features of nickel-based superalloy with temperature and strain rate along depth direction (Reprinted from [117], Copyright (2019), with permission from Elsevier).

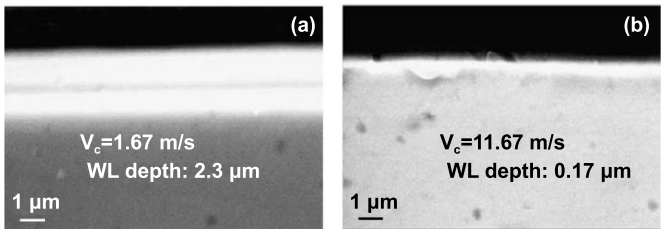

Figure 10. Variations in WL depth of H13 tool steel at two different turning speeds, V_c; WL depths are (a) 2.3μm and (b) 0.17μm (Reprinted from [120], Copyright (2006), with permission from Elsevier).

when the cutting speed was 1.67 m s^{-1}. When the cutting speed was increased to 11.67 m s^{-1}, the WL depth decreases to 0.17 μm. This decrease can be explained by the synergy among the influential factors of heat transfer, heat generation, and material softening at the top layer of the subsurface. An explanation is provided in figure 11.

The metallurgical microstructural evolution in the subsurface, which is strongly affected by the local temperature. The factors affecting the local temperature per unit volume are shown in figure 11(a). High local temperatures originate from mechanical work, specifically plastic work and the friction between cutter and workpiece. Another important factor is heat transfer, which involves the flow of heat in and out of the unit volume. Based on Fourier's law of heat conduction, the heat flux transfer is determined by the temperature gradient and material thermal conductivity. With increasing machining speed, the temperature gradient along the depth, and the machining process becomes adiabatic. Heat then aggregates at the top layer and induces high temperature and high-temperature gradients at the top layer along the depth direction. The high temperature causes local material softening at the top layer, and the high temperature gradient results in the rapid cooling at the top layer after machining based on Fourier's law of heat conduction.

In 1999, Chou and Evans [45] discovered the relationship between WL depth and cutting speed. This finding is shown in figure 11(c). Bosheh and Matrivenga [120] suggested that the WL depth decreased with increasing machining speeds because the duration of the cutting force on the unit material in the subsurface was shortened in HSM. However, this interpretation cannot explain why the WL depth increases at a relatively low machining speed, as shown in figure 11(c). Accordingly, we propose a mechanism based on the thermo-mechanical coupling relationship shown in figure 11(a).

The underlying mechanism of the variation in the WL depth consists of two parts. Strain rate affects the M-WL depth at relatively low machining speeds, and the adiabatic effect (heat) governs the T-WL depth at relatively high machining speeds as figure 11(c). The stress corresponding to low machining speeds varies with depth shown in figure 11(b)-I. The stress at the top layer of the subsurface increases with the machining speed. This increase in stress can be explained by the high strain rate induced by high machining speeds. The higher the machining speed, the greater the stress at the top layer. The greater stress at the top layer causes the greater stress at deeper locations. Once the local stress at deeper locations exceeds

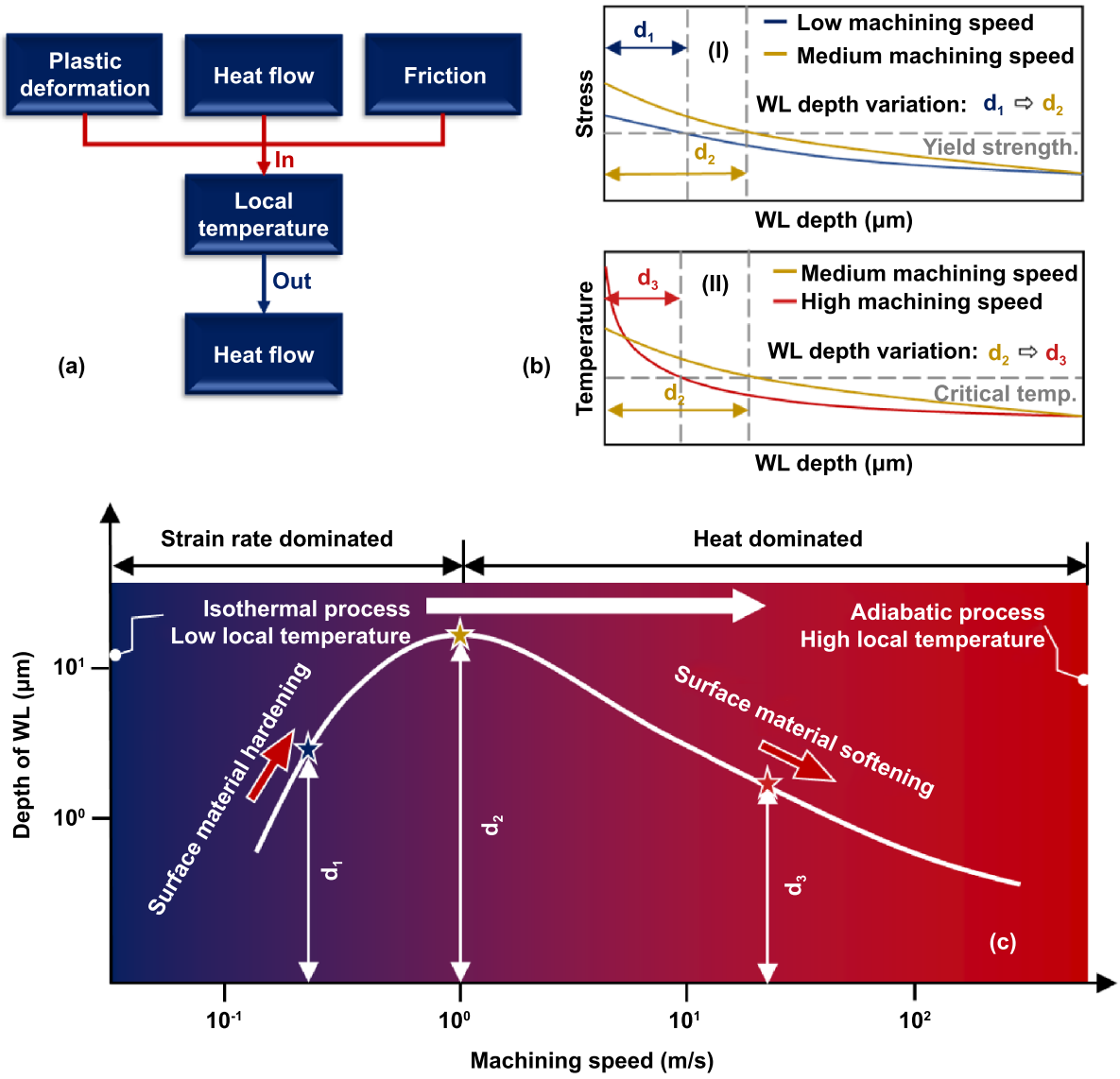

Figure 11. Mechanism of WL depth affected by machining speed: (a) thermo-mechanical coupling relationship in subsurface; (b) temperature distribution variation in subsurface with cutting speed; and (c) WL depth variation with machining speed based on results of Chou and Evans (Reprinted from [45], Copyright (1999), with permission from Elsevier).

the material yield strength, the local site becomes part of the M-WL. Hence, higher machining speeds result in deeper M-WLs. The temperature varying with depth corresponding to high machining speeds is illustrated in figure 11(b)-II. As the machining speed increases, the adiabatic effect causes the temperature at the top layer of the subsurface to increase considerably. A high local temperature results in material softening, which further causes the sharp decrease in the local yield strength. A low yield strength results in a decrease in local stress. Besides, the adiabatic effect does not allow heat to flow to deep locations. This means that material softening does not occur at deep locations, and the local yield strength does not decrease at deep locations. Therefore, the stress transmitted from the top layer to deep locations is insufficient to reach the local yield strength of the materials at deep locations, and the depth of the T-WL is confined within the region affected by the adiabatic effect. The increasing machining speed intensifies the adiabatic effect, and the depth of the T-WL decreases.

The adiabatic effect on subsurface damage in the HSM is corroborated by the grinding experiments conducted by Zhou *et al* [122]. As shown in figure 12(a), thermal-induced material softening reduces the shear stress transmitted to deep locations with increasing machining speed. The plastic deformation at the subsurface of A1199 aluminum at two machining speeds is characterized in figures 12(b) and (c). The figure indicates that plastic deformation flow lines occur when the machining speed is 20 m s^{-1}. However, these flow lines disappear when the machining speed is increased to 280 m s^{-1}, demonstrating that the material softening at the top layer of the subsurface relieves the local stress. Consequently, the shear stress transmitted to the subsurface further decreases to a value less than the local yield strength. A similar phenomenon occurs in the 5056 aluminum alloy, as shown in figures 12(d) and (e).

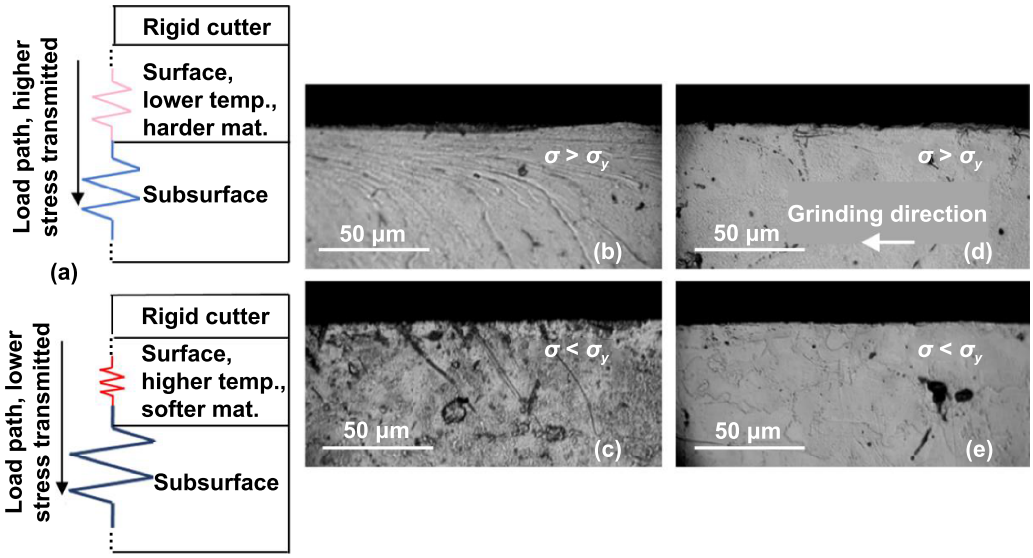

Figure 12. Mechanism of plastic deformation eliminated from subsurface: (a) material softening at load path; (b) and (c) subsurface characterization of A1199 aluminum ; and (d) and (e) subsurface characterization of 5056 aluminum alloy (Reprinted from [122], Copyright (2003), with permission from Elsevier).

Cracks, amorphous structures, and shear defects are the main metallurgical microstructural evolutions of brittle materials in HSM. In 2003, Huang and Liu [123] conducted HSM experiments on Al_2O_3 and found that lateral cracks were the major damage found in the subsurface at a grinding speed of 160 m s^{-1}. Nevertheless, no amorphous structure was confirmed in this study. Zhao *et al* discovered amorphous band structure can be created through initially forming stacking faults [88] in shocking single-crystalline silicon. In HSM, similar shear bands were discovered in various materials. In 1994, Puttick *et al* [124] found that shear bands existed in the subsurface of the crystalline silicon machined by nano-single-point turning (figure 13(a)). These shear bands were considered to be formed by dislocations gliding in slip systems. The occurrence of the shear bands at the machined subsurface of the ZERODUR glass was first reported by Schinker [125] in 1991. Shear bands were observed at the subsurface of the ZERODUR glass when the machining speed is 20 m s^{-1} (figure 13(b)). In 2020, shear bands were discovered in the subsurface of ground yttrium aluminum garnet (YAG) [44] (figure 13(d)). The metallurgical structure within the shear bands was confirmed as stacking faults. In 2016, Goel *et al* [126] conducted an MD simulation to confirm the existence of these shear bands (figure 13(c)). Similar simulation results were obtained by Liu *et al* [127] in 2021. In the simulations, amorphous is the metallurgical structure in these bands. However, one question regarding the shear band is whether the shear bands can be deemed as ASBs.

The first is that these shear bands are not caused by vibrations of the machine tool, because the band frequencies are in the range 0.1–10 MHz [125], which is higher than the frequency range of a typical machine tool. In HSM, the shear band is caused by shear stress, and adiabatic effect should be confined within the narrow bands. Therefore, we suggest that the shear bands be categorized as a type of ASB. Nevertheless, the amorphous structure was not formed within the shear bands of some types of materials, i.e. YAG. The reason is probably that the stress within the shear bands in HSM does not reach the threshold stress of forming amorphous structure. Because the transformation from diamond structure to amorphous needs high pressures. For example, Zhang and Zarudi [128] stated that the transformation of single-crystalline silicon from diamond structure to amorphous structure needs the octahedra stress reaching 4.8 GPa, and the pressure in the shock experiments of Zhao *et al* [88] reaches 11.2 GPa to form amorphous.

3.4. Material microstructural evolution in shock

UHSM cannot be achieved by the current experimental technology. Fortunately, many experiments and simulations have focused on the microstructural evolution during shock. The microstructural evolution of the materials in these studies can be used to speculate on how material microstructures evolve in UHSM. This section reviews the EFG and dislocation behavior under shocks. Subsequently, the formation of amorphous bands in brittle materials subjected to shock is reviewed.

After subjecting ductile materials to shock, the EFGs caused by DRX were observed. These materials include FCC materials (such as Cu [39] and 304 stainless steel [40]) and BCC materials (such as Fe [129] and W-Ta [130]). A post-mortem characterization of the crater-impacting test samples is presented in figure 14. In figure 14(a), the crater is shocked by a projectile at a speed of 3.3 km s^{-1}. The rim of the crater, usually considered to be pressure-driven, is curled. Location 'b' in the bright field image shown in figure 14(a) is characterized by transmission electron microscopy (figure 14(b)). As shown in figure 14(b), several EFGs occur at location 'b' with few other defects. This shows that DRX dominates the microstructural evolution at locations subjected to shock when

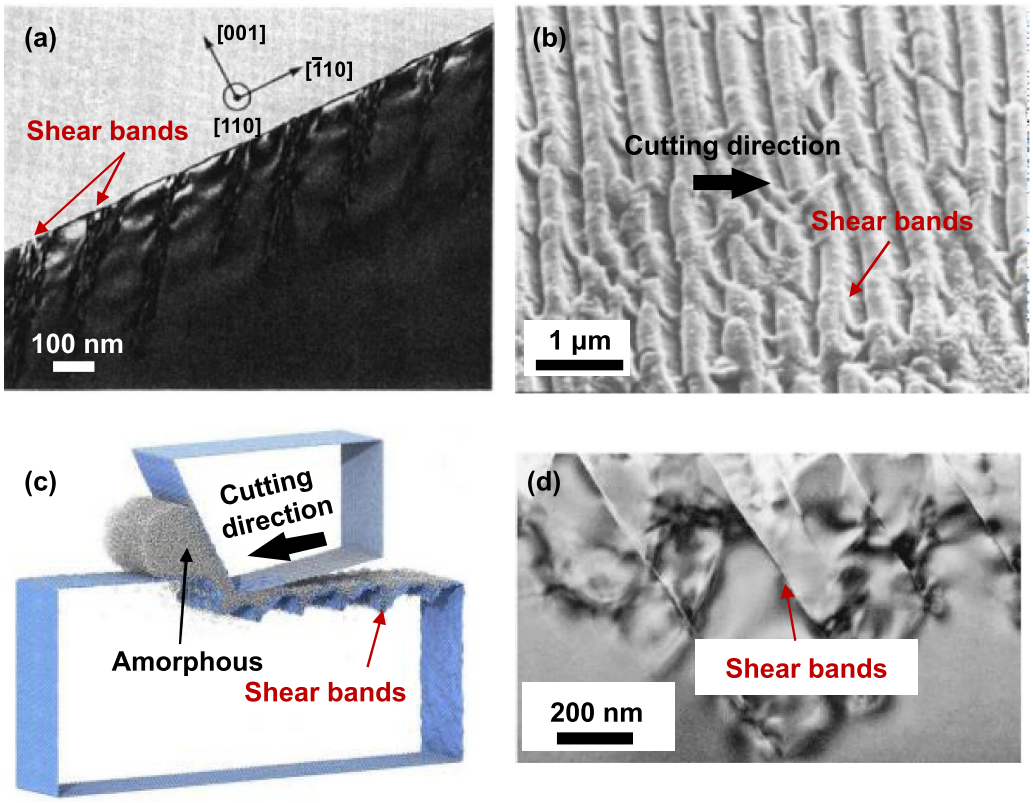

Figure 13. Shear bands in subsurface of brittle materials: (a) shear bands in subsurface of single-crystal silicon observed at cross-sectional plane ([124] Taylor & Francis Ltd http://tandfonline.com); (b) shear bands in subsurface of ZERODUR glass ceramic observed at surface plane [125] Reprinted from [125], Copyright (1991), with permission from Elsevier); (c) shear bands in single-crystalline silicon calculated by MD simulation on plane (Reprinted from [126], Copyright (2016), with permission from Elsevier); and (d) shear bands in subsurface of yttrium aluminum garnet (Reprinted from [44], Copyright (2019), with permission from Elsevier [44, 124] Taylor & Francis Ltd http://tandfonline.com. Reprinted from [125], Copyright (1991), with permission from Elsevier. Reprinted from [126], Copyright (2016), with permission from Elsevier. Reprinted from [44], Copyright (2019), with permission from Elsevie.

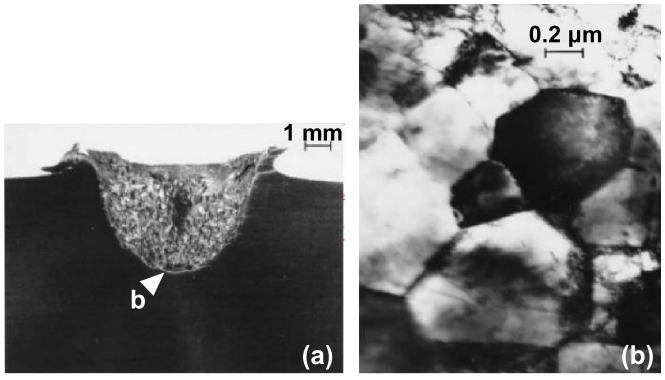

Figure 14. Crater in iron target was impacted by steel projectile at an impact speed of 3.3 km s^{-1}: (a) cross-section of iron crater and (b) nanoscale grains caused by DRX at crater wall shown in (a) (Reprinted by permission from Springer Nature Customer Service Centre GmbH: Springer Nature [41], Copyright (2004)).

temperatures are sufficiently high. The temperature at these locations accompanied by severe plastic deformation probably approximates the melting point during the transient period.

On the atomistic scale, the dynamic behavior of dislocations under shock has played a central role in previous studies. The mechanism by which dislocation, twinning, and atomistic decohesion dominate different strain rate ranges is provided by Hahn *et al* [131] based on MD, as shown in figure 15(a). In this figure, the spall strengths of the single crystal and nanocrystal tantalum at distinct strain rates are plotted. The spall strength increased until it reached the maximum spall strength at a strain rate comparable to the Debye frequency. Three types of microstructural evolution dominate the strain rate ranges. Dislocation dominates the structural evolution of tantalum when the strain rate is less than 10^7 1 s^{-1}. When the strain rate range is 10^7–10^9 1 s^{-1}, twinning becomes the main factor in microstructural evolution. Once the strain rate exceeds 10^9 1 s^{-1}, de-cohesion plays a major role. These microstructural transitions occur not only in tantalum but also in other materials [131]. The transitions are considered as competition between dislocations, twinning, and atomistic de-cohesion. In 2001, Meyers *et al* [132] proposed a theoretical equation to describe the competition between dislocation and twinning based on the critical driving stress. Their idea is that twinning and dislocation gliding only occur under the condition that the critical stress is satisfied. Therefore, the transition between dislocation gliding and twinning must occur when the critical stresses of dislocation gliding and twinning nucleation are equal. The critical stress of dislocation gliding can be obtained from the

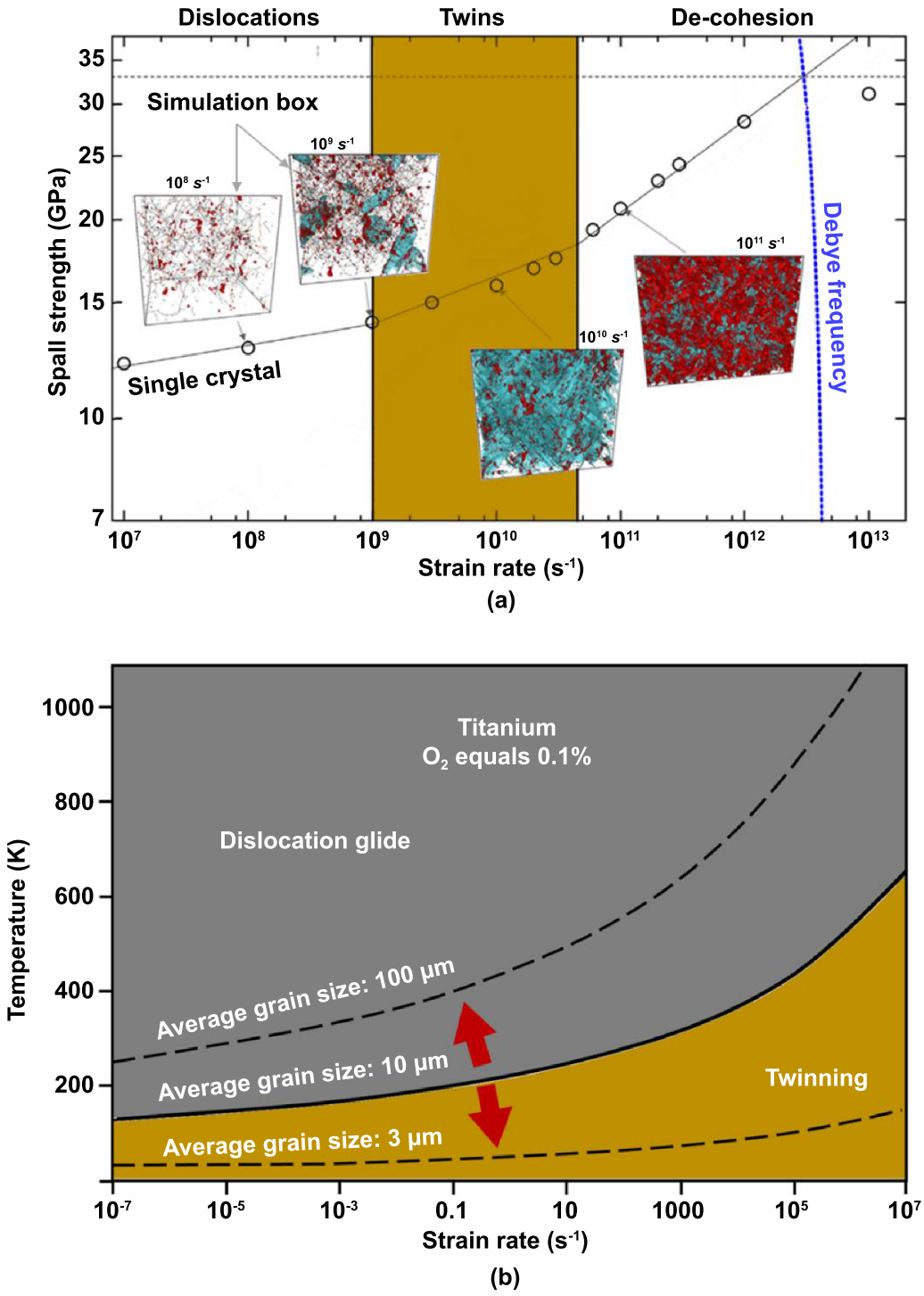

Figure 15. Micro-structural evolution variation with strain rate: (a) micro-structural evolution of tantalum with strain rate calculated from MD (Reprinted from [131], Copyright (2017), with permission from Elsevier); the dark lines in simulation boxes represents dislocation; the sky-blue marks stands for twinning; the deep-red marks means the surfaces of the voids caused by de-cohesion; (b) competition between twinning and dislocation based on relationship proposed by Meyers *et al* (Reprinted from [132], Copyright (2001), with permission from Elsevier).

Zerilli–Armstrong (Z–A) constitutive equation, and the critical stress for twinning nucleation can be obtained from the work of Johnston and Gilman [133]. The transition can be plotted as a critical curve that divides the strain rate–temperature phase diagram into two domains, as shown in figure 15(b). The upper domain represents the condition in which dislocation gliding occurs, and the lower domain represents the location where twinning occurs in the tantalum. Three curves with different grain sizes are plotted owing to the introduction of the Hall–Petch relationship by the Z–A constitutive equation. As

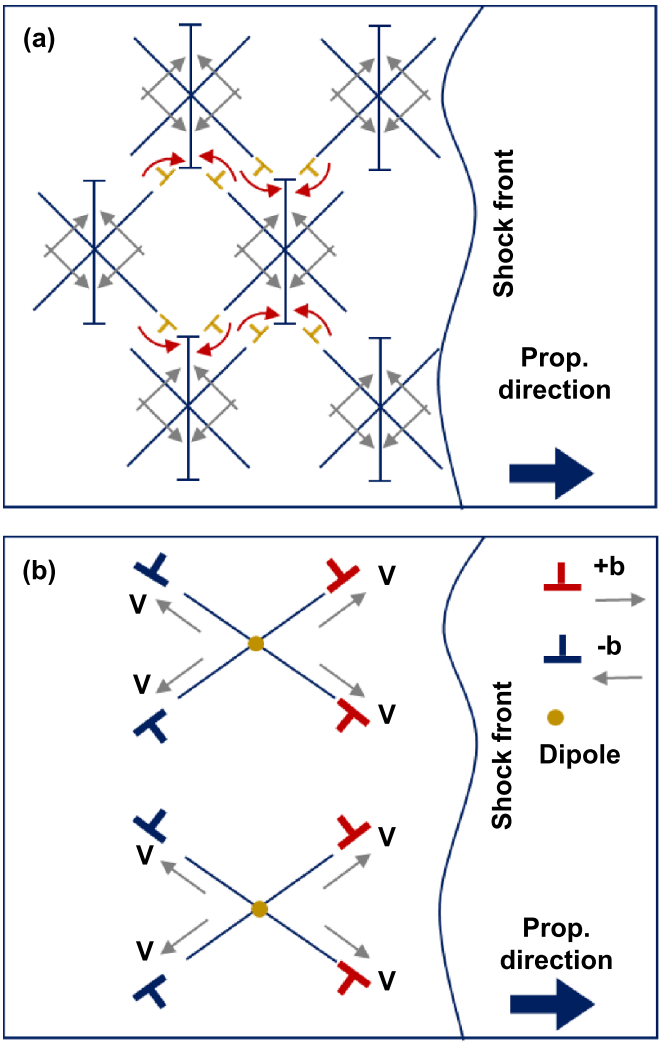

Figure 16. Dislocation multiplication behind shock front: models proposed by (a) Armstrong *et al* [137] and (b) Meyers [136].

shown in figure 15(b), twinning tends to be generated with large grain sizes. This phenomenon was observed in Cu by Murr and Esquivel [41].

Over the past decades, the dislocation multiplication behind the shock front has been another popular topic. The Frank–Read source and kink pair multiplication are usually the main sources of dislocation multiplication at low strain rates. However, the dislocation multiplication behind the shock front is typically based on homogeneous nucleation. More than half a century passed before researchers could disclose the evolution of dislocations behind shock fronts. In 1958, Smith [134] proposed a model involving an array of dislocations at the shock front. This array is the interface that separates compressed and uncompressed materials. In the model, the array is assumed to move with shock propagation. This model was modified by Hornbogen [135] because the dislocation substructure observed in the experiments could not be fully explained by Smith's model. In the Smith–Hornbogen model, dislocations are required to have supersonic velocity because the shock front can move at supersonic speeds to create high shock pressures. Moreover, the dislocations must have the same velocity as the shock front. However, this presumed supersonic velocity of dislocations has not been experimentally observed to date. Meyers *et al* [136] proposed a model in which dislocations nucleate homogeneously at the shock front. These nucleated dislocations left by the shock front only moved along a short distance. Newly nucleated dislocations are the Interfaces between uncompressed and compressed materials. This model does not require a dislocation with supersonic velocity to match the shock front. In 2007, Armstrong *et al* [137] proposed the model shown in figure 16(a). These resident partial dislocations behind the shock front glide along the maximum shear direction and react to form a dislocation in which the Burgers vector is parallel to the wave propagation. The newly nucleated dislocations relaxed the stresses at the shock front. In 2015, Gurrutxaga-Lerma *et al* [138] simulated the dislocation nucleation process at the shock front. Their study results are shown in figure 16(b). One dipole shown in figure 16(b) generates two types of dislocations: shielding and anti-shielding dislocations. The shielding dislocation, marked in red, shields the shock front, relaxing the shock compressive stress at the shock

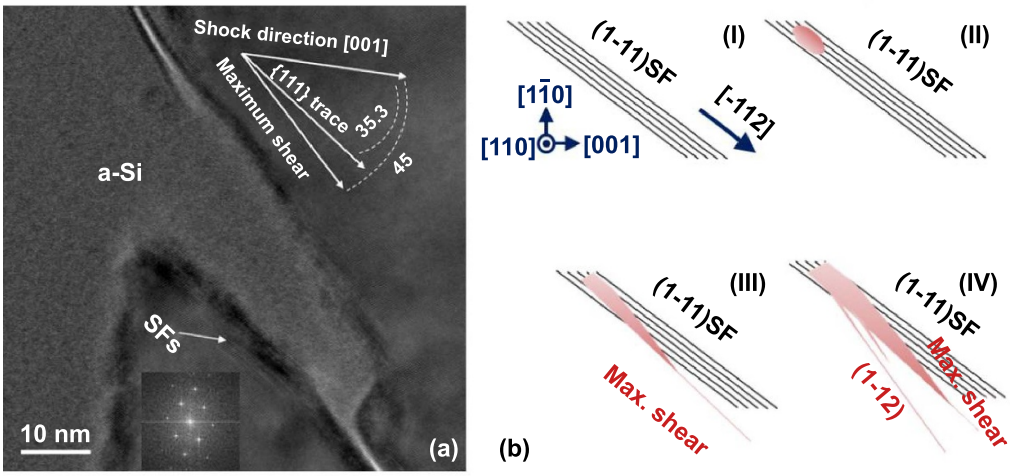

Figure 17. Mechanism of formation of amorphous ASBs: (a) occurrence of amorphous shear band in single-crystalline silicon subjected to shock; (b) schematic of mechanism of amorphous shear band nucleation (Reprinted from [88], Copyright (2016), with permission from Elsevier).

front. The anti-shielding dislocation, marked in blue, moves antiparallel to the shock propagation direction. To date, all proposed models remain at the theoretical stage. Experimental confirmation remains necessary in the future.

Amorphization is the major microstructural evolution of brittle materials during shock. These materials include Si [88, 139], Ge [140], SiC [141], and B_4C [142]. The underlying mechanism of amorphization was explained by Zhao *et al* [88]. In their study, stacking faults are found at the interface between amorphous ASBs and bulk materials, as shown in figure 17(a). These stacking faults provide an idea as to the origin of the amorphous bands. Zhao *et al* assumed that stacking faults are initially generated on the (111) plane of $(1\bar{1}1)$ before the amorphous onset, as shown in figure 17(b)-I. The angle between plane $(1\bar{1}1)$ and shock direction $[001]$ is 35.3°, whereas the maximum shear direction is 45° with respect to the shock direction, as shown in figure 17(b)-III. The deviation between these two angles results in the disorder of the atoms constituting the stacking faults, indicating that an amorphous phase is generated. With the development of the amorphous ASB, the amorphous shear band generated along $(1\bar{1}\bar{2})$ were observed.

4. Conclusions

This article briefly reviews the solid mechanics framework of ASB and the microstructural evolution at the subsurface and ASBs of chips in HSM. The review summary is as follows.

(1) Several metallurgical microstructure evolutions, including DRX, twinning, and phase transformation, have not yet been considered in current physics-based constitutive equations. Thus, more comprehensive physics-based constitutive equations must be proposed in the future.
(2) Several ASB onset criteria have been established over the past several decades. These criteria mainly describe the occurrence of ASBs when the loading rate is increased. However, ASBs can be depressed and subsequently eliminated when the loading rate is sufficiently high to cause shock. Therefore, in the future, the criteria of determining the transition from ASBs to shock needs to be established.
(3) The mechanical and thermal effects dominate the WL depth at low and high machining speeds, respectively. The mechanical and thermal effects increase and decrease the WL depth, respectively.

Acknowledgments

The authors wish to acknowledge the support of the Shenzhen Science and Technology Innovation Commission under Project Numbers KQTD20190929172505711, JSGG20210420091802007, and JCYJ20210324115413036, and Guangdong Provincial Department of Science and Technology under Project Number K22333004.

ORCID iD

Bi Zhang https://orcid.org/0000-0001-5738-3266

References

[1] Shaw M C and Cookson J O 2005 *Metal Cutting Principles* (New York: Oxford University)
[2] Salomon C J 1931 Process for machining metals of similar acting materials when being worked by cutting tools *German Patent* 523594
[3] Longbottom J M and Lanham J D 2006 A review of research related to Salomon's hypothesis on cutting speeds and temperatures *Int. J. Mach. Tools Manuf.* **46** 1740–7
[4] Zener C and Hollomon J H 1944 Effect of strain rate upon plastic flow of steel *J. Appl. Phys.* **15** 22–32
[5] Wright T W and Batra R C 1985 The initiation and growth of adiabatic shear bands *Int. J. Plast.* **1** 205–12

[6] Davies M A, Burns T J and Evans C J 1997 On the dynamics of chip formation in machining hard metals *CIRP Ann.* **46** 25–30

[7] Burns T J and Davies M A 2002 On repeated adiabatic shear band formation during high-speed machining *Int. J. Plast.* **18** 487–506

[8] Ma W, Chen X and Shuang F 2017 The chip-flow behaviors and formation mechanisms in the orthogonal cutting process of Ti6Al4V alloy *J. Mech. Phys. Solids* **98** 245–70

[9] Ma W, Li X, Dai L and Ling Z 2012 Instability criterion of materials in combined stress states and its application to orthogonal cutting process *Int. J. Plast.* **30–31** 18–40

[10] Cai S L and Dai L H 2014 Suppression of repeated adiabatic shear banding by dynamic large strain extrusion machining *J. Mech. Phys. Solids* **73** 84–102

[11] Ye G G, Xue S F, Jiang M Q, Tong X H and Dai L H 2013 Modeling periodic adiabatic shear band evolution during high speed machining Ti-6Al-4V alloy *Int. J. Plast.* **40** 39–55

[12] Ye G G, Xue S F, Ma W, Jiang M Q, Ling Z, Tong X H and Dai L H 2012 Cutting AISI 1045 steel at very high speeds *Int. J. Mach. Tools Manuf.* **56** 1–9

[13] Gurrutxaga-Lerma B 2018 Adiabatic shear banding and the micromechanics of plastic flow in metals *Int. J. Solids Struct.* **132** 153–70

[14] Bai Y L 1982 Thermo-plastic instability in simple shear *J. Mech. Phys. Solids* **30** 195–207

[15] Recht R F 1964 Catastrophic thermoplastic shear *J. Appl. Mech.* **31** 189–93

[16] Ye G G, Jiang M Q, Xue S F, Ma W and Dai L H 2018 On the instability of chip flow in high-speed machining *Mech. Mater.* **116** 104–19

[17] Regazzoni G, Kocks U F and Follansbee P S 1987 Dislocation kinetics at high strain rates *Acta Metall.* **35** 2865–75

[18] Meyers M A 1994 *Dynamic Behavior of Materials* (New York: Wiley)

[19] Zerilli F J and Armstrong R W 1992 The effect of dislocation drag on the stress-strain behavior of F.C.C. metals *Acta Metall. Mater.* **40** 1803–8

[20] Follansbee P S and Kocks U F 1988 A constitutive description of the deformation of copper based on the use of the mechanical threshold stress as an internal state variable *Acta Metall.* **36** 81–93

[21] Parameswaran V R, Urabe N and Weertman J 1972 Dislocation mobility in aluminum *J. Appl. Phys.* **43** 2982–6

[22] Gurrutxaga-Lerma B, Balint D S, Dini D and Sutton A P 2015 The mechanisms governing the activation of dislocation sources in aluminum at different strain rates *J. Mech. Phys. Solids* **84** 273–92

[23] Gao C Y and Zhang L C 2012 Constitutive modelling of plasticity of fcc metals under extremely high strain rates *Int. J. Plast.* **32–33** 121–33

[24] Gurson A L 1977 Continuum theory of ductile rupture by void nucleation and growth: part I—yield criteria and flow rules for porous ductile media *J. Eng. Mater. Technol.* **99** 2–15

[25] Seaman L, Curran D R and Shockey D A 1976 Computational models for ductile and brittle fracture *J. Appl. Phys.* **47** 4814–26

[26] Tvergaard V and Needleman A 1984 Analysis of the cup-cone fracture in a round tensile bar *Acta Metall.* **32** 157–69

[27] Rudd R E and Belak J F 2002 Void nucleation and associated plasticity in dynamic fracture of polycrystalline copper: an atomistic simulation *Comput. Mater. Sci.* **24** 148–53

[28] Seppälä E T, Belak J and Rudd R E 2004 Effect of stress triaxiality on void growth in dynamic fracture of metals: a molecular dynamics study *Phys. Rev.* B **69** 134101

[29] Seppälä E T, Belak J and Rudd R E 2005 Three-dimensional molecular dynamics simulations of void coalescence during dynamic fracture of ductile metals *Phys. Rev.* B **71** 064112

[30] Sills R B and Boyce B L 2020 Void growth by dislocation adsorption *Mater. Res. Lett.* **8** 103–9

[31] Traiviratana S, Bringa E M, Benson D J and Meyers M A 2008 Void growth in metals: atomistic calculations *Acta Mater.* **56** 3874–86

[32] Nguyen L D and Warner D H 2012 Improbability of void growth in aluminum via dislocation nucleation under typical laboratory conditions *Phys. Rev. Lett.* **108** 035501

[33] Rice J R and Tracey D M 1969 On the ductile enlargement of voids in triaxial stress fields *J. Mech. Phys. Solids* **17** 201–17

[34] Huang Y 1991 Accurate dilatation rates for spherical voids in triaxial stress fields *J. Appl. Mech.* **58** 1084–6

[35] Hosseini S B, Klement U, Yao Y and Ryttberg K 2015 Formation mechanisms of white layers induced by hard turning of AISI 52100 steel *Acta Mater.* **89** 258–67

[36] Rogers H C 1979 Adiabatic plastic deformation *Annu. Rev. Mater. Sci.* **9** 283–311

[37] Meyers M A, Xu Y B, Xue Q, Pérez-Prado M T and McNelley T R 2003 Microstructural evolution in adiabatic shear localization in stainless steel *Acta Mater.* **51** 1307–25

[38] Duan C Z and Zhang L C 2012 Adiabatic shear banding in AISI 1045 steel during high speed machining: mechanisms of microstructural evolution *Mater. Sci. Eng.* A **532** 111–9

[39] Murr L E, Quinones S A, Ferreyra E, Ayala A, Valerio O L, Hörz F and Bernhard R P 1998 The low-velocity-to-hypervelocity penetration transition for impact craters in metal targets *Mater. Sci. Eng.* A **256** 166–82

[40] Murr L E, Trillo E A, Bujanda A A and Martinez N E 2002 Comparison of residual microstructures associated with impact craters in fcc stainless steel and bcc iron targets: the microtwin versus microband issue *Acta Mater.* **50** 121–31

[41] Murr L E and Esquivel E V 2004 Observations of common microstructural issues associated with dynamic deformation phenomena: twins, microbands, grain size effects, shear bands, and dynamic recrystallization *J. Mater. Sci.* **39** 1153–68

[42] Gao S, Wu Y, Kang R and Huang H 2018 Nanogrinding induced surface and deformation mechanism of single crystal β-Ga_2O_3 *Mater. Sci. Semicond. Process.* **79** 165–70

[43] Li C, Wu Y, Li X, Ma L, Zhang F and Huang H 2020 Deformation characteristics and surface generation modelling of crack-free grinding of GGG single crystals *J. Mater. Process. Technol.* **279** 116577

[44] Li C, Li X, Wu Y, Zhang F and Huang H 2019 Deformation mechanism and force modelling of the grinding of YAG single crystals *Int. J. Mach. Tools Manuf.* **143** 23–37

[45] Chou Y K and Evans C J 1999 White layers and thermal modeling of hard turned surfaces *Int. J. Mach. Tools Manuf.* **39** 1863–81

[46] Ramesh A, Melkote S N, Allard L F, Riester L and Watkins T R 2005 Analysis of white layers formed in hard turning of AISI 52100 steel *Mater. Sci. Eng.* A **390** 88–97

[47] Schulz H and Moriwaki T 1992 High-speed machining *CIRP Ann.* **41** 637–43

[48] Klocke F, Brinksmeier E, Evans C, Howes T, Lnasaki I, Minke E, Tönshoff H K, Webster J A and Stuff D 1997 High-speed grinding-fundamentals and state of the art in Europe, Japan, and the USA *CIRP Ann.* **46** 715–24

[49] Dudzinski D, Devillez A, Moufki A, Larrouquère D, Zerrouki V and Vigneau J 2004 A review of developments towards dry and high speed machining of Inconel 718 alloy *Int. J. Mach. Tools Manuf.* **44** 439–56

[50] Rahman M, Wang Z-G and Wong Y-S 2006 A review on high-speed machining of titanium alloys *JSME Int. J. Ser.* C **49** 11–20

[51] Yang X and Zhang B 2019 Material embrittlement in high strain-rate loading *Int. J. Extrem. Manuf.* **1** 022003

[52] Zhang T, Jiang F, Huang H, Lu J, Wu Y, Jiang Z and Xu X 2021 Towards understanding the brittle–ductile transition in the extreme manufacturing *Int. J. Extrem. Manuf.* **3** 022001

[53] Zhang B and Yin J 2019 The 'skin effect' of subsurface damage distribution in materials subjected to high-speed machining *Int. J. Extrem. Manuf.* **1** 012007

[54] Wang B, Liu Z, Cai Y, Luo X, Ma H, Song Q and Xiong Z 2021 Advancements in material removal mechanism and surface integrity of high speed metal cutting: a review *Int. J. Mach. Tools Manuf.* **166** 103744

[55] Molinari A, Soldani X and Miguélez M H 2013 Adiabatic shear banding and scaling laws in chip formation with application to cutting of Ti–6Al–4V *J. Mech. Phys. Solids* **61** 2331–59

[56] Hou X, Li J, Li Y and Tian Y 2022 Intermolecular and surface forces in atomic-scale manufacturing *Int. J. Extrem. Manuf.* **4** 022002

[57] Gao J, Luo X, Fang F and Sun J 2021 Fundamentals of atomic and close-to-atomic scale manufacturing: a review *Int. J. Extrem. Manuf.* **4** 012001

[58] Peierls R 1940 The size of a dislocation *Proc. Phys. Soc.* **52** 34

[59] Nabarro F R N 1947 Dislocations in a simple cubic lattice *Proc. Phys. Soc.* **59** 256

[60] Hull D and Bacon D J 2001 *Introduction to Dislocations* (Oxford: Butterworth-Heinemann)

[61] Messerschmidt U 2010 *Dislocation Dynamics during Plastic Deformation* (Heidelberg: Springer Science & Business Media)

[62] Wedberg D and Lindgren L-E 2015 Modelling flow stress of AISI 316L at high strain rates *Mech. Mater.* **91** 194–207

[63] Zerilli F J and Armstrong R W 1987 Dislocation-mechanics-based constitutive relations for material dynamics calculations *J. Appl. Phys.* **61** 1816–25

[64] Hoge K G and Mukherjee A K 1977 The temperature and strain rate dependence of the flow stress of tantalum *J. Mater. Sci.* **12** 1666–72

[65] Steinberg D J and Lund C M 1989 A constitutive model for strain rates from 10^{-4} to 10^{6} s^{-1} *J. Appl. Phys.* **65** 1528–33

[66] Taylor G I 1934 The mechanism of plastic deformation of crystals. Part I.—theoretical *Proc. R. Soc.* A **145** 362–87

[67] De Cooman B C, Estrin Y and Kim S K 2018 Twinning-induced plasticity (TWIP) steels *Acta Mater.* **142** 283–362

[68] Zaefferer S, Ohlert J and Bleck W 2004 A study of microstructure, transformation mechanisms and correlation between microstructure and mechanical properties of a low alloyed TRIP steel *Acta Mater.* **52** 2765–78

[69] Johnson G R and Cook W H 1985 Fracture characteristics of three metals subjected to various strains, strain rates, temperatures and pressures *Eng. Fract. Mech.* **21** 31–48

[70] Klopp R W, Clifton R J and Shawki T G 1985 Pressure-shear impact and the dynamic viscoplastic response of metals *Mech. Mater.* **4** 375–85

[71] Gioia G and Ortiz M 1996 The two-dimensional structure of dynamic boundary layers and shear bands in thermoviscoplastic solids *J. Mech. Phys. Solids* **44** 251–92

[72] Molinari A and Clifton R J 1987 Analytical characterization of shear localization in thermoviscoplastic materials *J. Appl. Mech.* 54 806–12

[73] Wright T W and Perzyna P 2003 Physics and mathematics of adiabatic shear bands *Appl. Mech. Rev.* **56** B41–B43

[74] Oxley P L B and Shaw M C 1990 Mechanics of machining: an analytical approach to assessing machinability *J. Appl. Mech.* **57** 253

[75] Johnson W 1983 *Impact Strength of Materials* (London: Edward Arnold)

[76] Perzyna P 1986 Internal state variable description of dynamic fracture of ductile solids *Int. J. Solids Struct.* **22** 797–818

[77] Tonks D L, Vorthman J E, Hixson R, Kelly A and Zurek A K 2001 Spallation studies on shock loaded U-6 WT PCT NB *AIP Conf. Proc.* **505** 329

[78] Sui H, Yu L, Liu W, Liu Y, Cheng Y and Duan H 2021 Theoretical models of void nucleation and growth for ductile metals under dynamic loading: a review *Matter Radiat. Extremes* **7** 018201

[79] Lyles R L and Wilsdorf H G F 1975 Microcrack nucleation and fracture in silver crystals *Acta Metall.* **23** 269–77

[80] Cuitino A M and Ortiz M 1996 Ductile fracture by vacancy condensation in fcc single crystals *Acta Mater.* **44** 427–36

[81] Reina C, Marian J and Ortiz M 2011 Nanovoid nucleation by vacancy aggregation and vacancy-cluster coarsening in high-purity metallic single crystals *Phys. Rev.* B **84** 104117

[82] Seppälä E T, Belak J and Rudd R E 2004 Onset of void coalescence during dynamic fracture of ductile metals *Phys. Rev. Lett.* **93** 245503

[83] Marian J, Knap J and Ortiz M 2004 Nanovoid cavitation by dislocation emission in aluminum *Phys. Rev. Lett.* **93** 165503

[84] Marian J, Knap J and Ortiz M 2005 Nanovoid deformation in aluminum under simple shear *Acta Mater.* **53** 2893–900

[85] Krasnikov V S and Mayer A E 2015 Plasticity driven growth of nanovoids and strength of aluminum at high rate tension: molecular dynamics simulations and continuum modeling *Int. J. Plast.* **74** 75–91

[86] Irwin G J 1972 *Metallographic Interpretation of Impacted Ogive Penetrators* (Ottawa: Defence Research Board)

[87] Kumagai T, Izumi S, Hara S and Sakai S 2007 Development of bond-order potentials that can reproduce the elastic constants and melting point of silicon for classical molecular dynamics simulation *Comput. Mater. Sci.* **39** 457–64

[88] Zhao S, Hahn E N, Kad B, Remington B A, Wehrenberg C E, Bringa E M and Meyers M A 2016 Amorphization and nanocrystallization of silicon under shock compression *Acta Mater.* **103** 519–33

[89] Teng X, Wierzbicki T and Couque H 2007 On the transition from adiabatic shear banding to fracture *Mech. Mater.* **39** 107–25

[90] Grady D 2017 *Physics of Shock and Impact* vol 1 (Bristol: IOP Publishing)

[91] Rankine W J M 1998 On the thermodynamic theory of waves of finite longitudinal disturbance [Philos. Trans. 160 (1870), part II, 277–288] *Classic Papers in Shock Compression Science, High-Press. Shock Compression Condens. Matter* pp 133–47

[92] Grüneisen E 1912 Theorie des festen Zustandes einatomiger Elemente *Ann. Phys.* **344** 257–306

[93] Anderson C E 1987 An overview of the theory of hydrocodes *Int. J. Impact Eng.* **5** 33–59

[94] Sutter G and List G 2013 Very high speed cutting of Ti–6Al–4V titanium alloy–change in morphology and mechanism of chip formation *Int. J. Mach. Tools Manuf.* **66** 37–43

[95] Sutter G 2005 Chip geometries during high-speed machining for orthogonal cutting conditions *Int. J. Mach. Tools Manuf.* **45** 719–26

[96] Sutter G, Faure L, Molinari A, Ranc N and Pina V 2003 An experimental technique for the measurement of temperature fields for the orthogonal cutting in high speed machining *Int. J. Mach. Tools Manuf.* **43** 671–8

[97] Zhou M, Rosakis A J and Ravichandran G 1996 Dynamically propagating shear bands in impact-loaded prenotched plates—I. Experimental investigations of temperature signatures and propagation speed *J. Mech. Phys. Solids* **44** 981–1006

[98] Timothy S P and Hutchings I M 1986 Adiabatic shear band fracture surfaces in a titanium alloy *J. Mater. Sci. Lett.* **5** 453–4

[99] Liao S and Duffy J 1998 Adiabatic shear bands in a TI-6Al-4V titanium alloy *J. Mech. Phys. Solids* **46** 2201–31

[100] Wang B, Sun J, Wang X and Fu A 2015 Adiabatic shear localization in a near beta Ti–5Al–5Mo–5 V–1Cr–1Fe alloy *Mater. Sci. Eng.* A **639** 526–33

[101] Wang B, Wang X, Li Z, Ma R, Zhao S, Xie F and Zhang X 2016 Shear localization and microstructure in coarse grained beta titanium alloy *Mater. Sci. Eng.* A **652** 287–95

[102] Xu Z, Junjia C and Guangyao L 2017 Microstructural mechanism in adiabatic shear bands of Al-Cu alloy bars using electromagnetic impact upsetting *Mater. Lett.* **194** 62–65

[103] Yang H, Zhang J H, Xu Y and Meyers M A 2008 Microstructural characterization of the shear bands in Fe-Cr-Ni single crystal by EBSD *J. Mater. Sci. Technol.* **24** 819

[104] Zou D L, Zhen L, Xu C Y and Shao W Z 2011 Characterization of adiabatic shear bands in AM60B magnesium alloy under ballistic impact *Mater. Charact.* **62** 496–502

[105] Kad B K, Gebert J-M, Perez-Prado M T, Kassner M E and Meyers M A 2006 Ultrafine-grain-sized zirconium by dynamic deformation *Acta Mater.* **54** 4111–27

[106] Peirs J, Tirry W, Amin-Ahmadi B, Coghe F, Verleysen P, Rabet L, Schryvers D and Degrieck J 2013 Microstructure of adiabatic shear bands in Ti6Al4V *Mater. Charact.* **75** 79–92

[107] Huang K and Logé R E 2016 A review of dynamic recrystallization phenomena in metallic materials *Mater. Des.* **111** 548–74

[108] Hines J A and Vecchio K S 1997 Recrystallization kinetics within adiabatic shear bands *Acta Mater.* **45** 635–49

[109] Meyers M A, Gregori F, Kad B K, Schneider M S, Kalantar D H, Remington B A, Ravichandran G, Boehly T and Wark J S 2003 Laser-induced shock compression of monocrystalline copper: characterization and analysis *Acta Mater.* **51** 1211–28

[110] Velásquez J D P, Bolle B, Chevrier P, Geandier G and Tidu A 2007 Metallurgical study on chips obtained by high speed machining of a Ti–6wt.%Al–4wt.%V alloy *Mater. Sci. Eng.* A **452–453** 469–74

[111] Derep J L 1987 Microstructure transformation induced by adiabatic shearing in armour steel *Acta Metall.* **35** 1245–9

[112] Duan C Z and Wang M J 2005 Characteristics of adiabatic shear bands in the orthogonal, cutting of 30CrNi$_3$MoV steel *J. Mater. Process. Technol.* **168** 102–6

[113] Xu Y, Zhang J, Bai Y and Meyers M A 2008 Shear localization in dynamic deformation: microstructural evolution *Metall. Mater. Trans.* A **39** 811–43

[114] Li Z, Wang B, Zhao S, Valiev R Z, Vecchio K S and Meyers M A 2017 Dynamic deformation and failure of ultrafine-grained titanium *Acta Mater.* **125** 210–8

[115] Hosseini S B, Ryttberg K, Kaminski J and Klement U 2012 Characterization of the surface integrity induced by hard turning of bainitic and martensitic AISI 52100 steel *Proc. CIRP* **1** 494–9

[116] Österle W and Li P X 1997 Mechanical and thermal response of a nickel-base superalloy upon grinding with high removal rates *Mater. Sci. Eng.* A **238** 357–66

[117] Liao Z, Polyakov M, Diaz O G, Axinte D, Mohanty G, Maeder X, Michler J and Hardy M 2019 Grain refinement mechanism of nickel-based superalloy by severe plastic deformation—mechanical machining case *Acta Mater.* **180** 2–14

[118] Velásquez J D P, Tidu A, Bolle B, Chevrier P and Fundenberger J-J 2010 Sub-surface and surface analysis of high speed machined Ti–6Al–4V alloy *Mater. Sci. Eng.* A **527** 2572–8

[119] Xu X, Zhang J, Liu H, He Y and Zhao W 2019 Grain refinement mechanism under high strain-rate deformation in machined surface during high speed machining Ti6Al4V *Mater. Sci. Eng.* A **752** 167–79

[120] Bosheh S S and Mativenga P T 2006 White layer formation in hard turning of H13 tool steel at high cutting speeds using CBN tooling *Int. J. Mach. Tools Manuf.* **46** 225–33

[121] Herbert C, Axinte D A, Hardy M and Withers P 2014 Influence of surface anomalies following hole making operations on the fatigue performance for a nickel-based superalloy *J. Manuf. Sci. Eng.* **136** 136–5

[122] Zhou L, Shimizu J, Muroya A and Eda H 2003 Material removal mechanism beyond plastic wave propagation rate *Precis. Eng.* **27** 109–16

[123] Huang H and Liu Y C 2003 Experimental investigations of machining characteristics and removal mechanisms of advanced ceramics in high speed deep grinding *Int. J. Mach. Tools Manuf.* **43** 811–23

[124] Puttick K E, Whitmore L C, Chao C L and Gee A E 1994 Transmission electron microscopy of nanomachined silicon crystals *Phil. Mag.* A **69** 91–103

[125] Schinker M G 1991 Subsurface damage mechanisms at high-speed ductile machining of optical glasses *Precis. Eng.* **13** 208–18

[126] Goel S, Kovalchenko A, Stukowski A and Cross G 2016 Influence of microstructure on the cutting behaviour of silicon *Acta Mater.* **105** 464–78

[127] Liu C, Chen X, Ke J, She Z, Zhang J, Xiao J and Xu J 2021 Numerical investigation on subsurface damage in nanometric cutting of single-crystal silicon at elevated temperatures *J. Manuf. Process.* **68** 1060–71

[128] Zhang L and Zarudi I 2001 Towards a deeper understanding of plastic deformation in mono-crystalline silicon *Int. J. Mech. Sci.* **43** 1985–96

[129] Murr L E, Bujanda A A, Trillo E A and Martinez N E 2002 Deformation twins associated with impact craters in polycrystalline iron targets *J. Mater. Sci. Lett.* **21** 559–63

[130] Trillo E A, Esquivel E V, Murr L E and Magness L S 2002 Dynamic recrystallization-induced flow phenomena in tungsten–tantalum (4%) [001] single-crystal rod ballistic penetrators *Mater. Charact.* **48** 407–21

[131] Hahn E N, Germann T C, Ravelo R, Hammerberg J E and Meyers M A 2017 On the ultimate tensile strength of tantalum *Acta Mater.* **126** 313–28

[132] Meyers M A, Vöhringer O and Lubarda V A 2001 The onset of twinning in metals: a constitutive description *Acta Mater.* **49** 4025–39

[133] Johnston W G and Gilman J J 1959 Dislocation velocities, dislocation densities, and plastic flow in lithium fluoride crystals *J. Appl. Phys.* **30** 129–44

[134] Smith C S 1958 Metallographic studies of metals after explosive shock *Trans. Met. Soc. AIME* **212**
[135] Hornbogen E 1962 Shock-induced dislocations *Acta Metall.* **10** 978–80
[136] Meyers M A 1978 A mechanism for dislocation generation in shock-wave deformation *Scr. Metall.* **12** 21–26
[137] Armstrong R W, Arnold W and Zerilli F J 2007 Dislocation mechanics of shock-induced plasticity *J. Metall. Mater. Trans.* A **38** 2605–10
[138] Gurrutxaga-Lerma B, Balint D S, Dini D, Eakins D E and Sutton A P 2015 The role of homogeneous nucleation in planar dynamic discrete dislocation plasticity *J. Appl. Mech.* **82** 82–7
[139] Zhao S, Kad B, Hahn E N, Remington B A, Wehrenberg C E, Huntington C M, Park H-S, Bringa E M, More K L and Meyers M A 2015 Pressure and shear-induced amorphization of silicon *Extreme Mech. Lett.* **5** 74–80
[140] Zhao S, Kad B, Wehrenberg C E, Remington B A, Hahn E N, More K L and Meyers M A 2017 Generating gradient germanium nanostructures by shock-induced amorphization and crystallization *Proc. Natl Acad. Sci.* **114** 9791–6
[141] Zhao S, Flanagan R, Hahn E N, Kad B, Remington B A, Wehrenberg C E, Cauble R, More K and Meyers M A 2018 Shock-induced amorphization in silicon carbide *Acta Mater.* **158** 206–13
[142] Zhao S, Kad B, Remington B A, LaSalvia J C, Wehrenberg C E, Behler K D and Meyers M A 2016 Directional amorphization of boron carbide subjected to laser shock compression *Proc. Natl Acad. Sci.* **113** 12088–93